

1 **What caused record-breaking aerosol loading over the South China** 2 **Sea in April 2023**

3 **Saginela Ravindra Babu^{1*} and Neng-Huei Lin^{1,2*}**

4 ¹Department of Atmospheric Sciences, National Central University, Taoyuan 32001, Taiwan.

5 ²Center for Environmental Monitoring and Technology, National Central University, Taoyuan
6 32001, Taiwan.

7 Correspondence to: S. Ravindra Babu (baburavindra595@gmail.com) and Neng-Huei Lin
8 (nhlin@cc.ncu.edu.tw).

9 **Abstract**

10 In April 2023, record-breaking aerosol optical depth (AOD) levels were observed over the South
11 China Sea (SCS). This study investigates the sources, transport pathways, and large-scale
12 dynamical conditions associated with this extreme aerosol event. Observations from the Moderate
13 Resolution Imaging Spectroradiometer (MODIS) revealed the highest April AOD in the 2003-
14 2023 satellite record, with values increasing by approximately 150% relative to the 2003-2022
15 climatological mean and exceeding 4σ above normal conditions. Enhanced carbon monoxide (CO)
16 concentrations were simultaneously detected in the free to mid-troposphere (700-500 hPa) by
17 Measurements of Pollution in the Troposphere (MOPITT) and Atmospheric Infrared Sounder
18 (AIRS), indicating substantial long-range transport of combustion-related pollution. MODIS fire
19 count and burned-area datasets further indicated intensified biomass-burning (BB) activity over
20 northern Peninsular Southeast Asia (PSEA) during the same period. Backward trajectory
21 simulations using the NOAA Hybrid Single-Particle Lagrangian Integrated Trajectory (HYSPLIT)
22 model suggested that a large fraction of air masses arriving over the SCS originated from northern
23 PSEA, supporting the interpretation that BB emissions from this region contributed substantially
24 to the elevated aerosol loading over the SCS. Dynamical analyses revealed a persistent anti-
25 cyclonic anomaly over northern PSEA at 500 hPa, accompanied by an eastward-shifted Bay of
26 Bengal anticyclone at 700 hPa and a western North Pacific cyclonic anomaly at both levels. These
27 circulation anomalies likely altered the prevailing regional flow by shifting climatological
28 southerlies toward northerly anomalies, thereby favoring aerosol transport and accumulation over
29 the SCS. Overall, the results suggest that the extreme aerosol event was associated with the
30 combined influence of intensified BB emissions and anomalous atmospheric circulation,

31 highlighting the important role of coupled emissions and atmospheric dynamics in shaping
32 regional aerosol extremes.

33 **Key words: Aerosol loading; South China Sea; MODIS; Biomass-burning**

34 **1. Introduction**

35 Atmospheric aerosols play a vital role in Earth’s climate by impacting radiation balance, cloud
36 microphysics, and air quality (Ramanathan et al., 2001; Anderson et al., 2003; Forster et al., 2021;
37 IPCC, 2023). These particles scatter and absorb solar radiation directly, influencing radiative
38 effects, and also modify cloud properties, lifespan, and precipitation by serving as nuclei for
39 condensation and ice formation. As a result, aerosols affect atmospheric thermodynamics, cloud–
40 radiation interactions, and the water cycle (Twomey et al., 1977; IPCC, 2023). Monitoring aerosol
41 levels over remote ocean regions is especially important because these areas provide a baseline for
42 natural background aerosol levels and help evaluate the effects of long-range transport on regional
43 climate through radiative and cloud processes (Pani et al., 2023). In addition to anthropogenic
44 emissions, natural events such as wildfires and agricultural biomass-burning (BB) are significant
45 episodic sources, emitting large quantities of aerosol particles and trace gases that substantially
46 affect both regional and global climate systems (Crutzen and Andreae, 1990; Ramanathan et al.,
47 2001; Lin et al., 2013; Reid et al., 2013; Kolden et al., 2024).

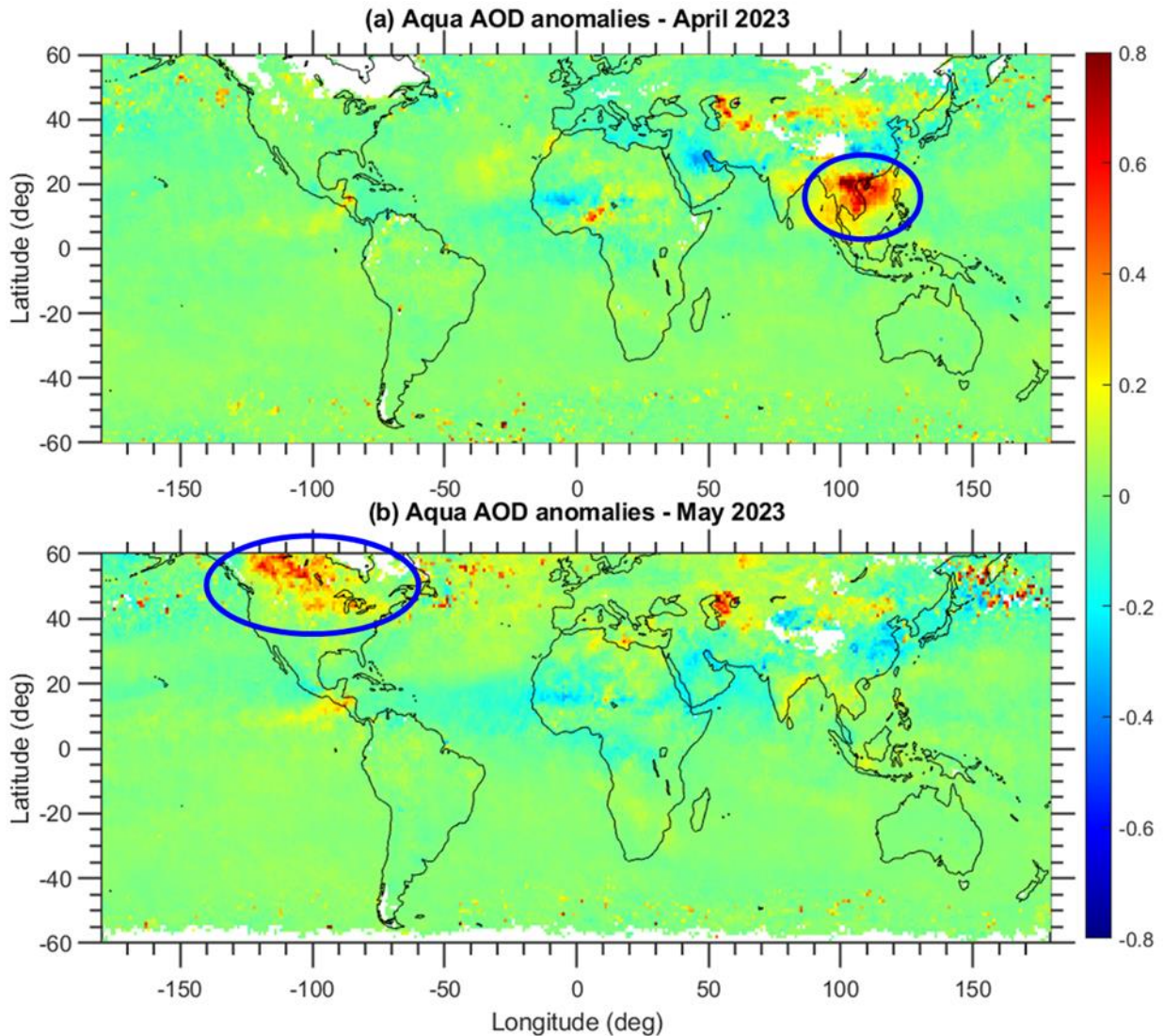
48 The South China Sea (SCS), situated in Asia, is the largest marginal sea in the tropical–
49 subtropical western North Pacific (WNP), serving as a vital natural laboratory for examining
50 aerosol variability in a relatively pristine marine environment (Reid et al., 2013; Lin et al., 2013;
51 Pani et al., 2023). Although it is an oceanic region, the atmosphere over the SCS is significantly
52 influenced by emissions from nearby continents and regional circulation patterns (Pani et al.,
53 2023). Typically, the SCS is dominated by a monsoon system, with the northeast monsoon
54 occurring during boreal winter and spring, and the southwest monsoon during boreal summer and
55 autumn (Cui et al., 2016). These seasonal wind patterns play a key role in aerosol transport, often
56 carrying natural and human-made pollutants from East Asia into the SCS basin over long distances.
57 In addition to continental outflow from East Asia, BB emissions from surrounding areas notably
58 influence aerosol concentrations over the SCS. During the summer monsoon months, particularly
59 August to October, persistent peatland and forest fires across the Maritime Continent (MC)
60 generate large smoke plumes that drift toward the southern SCS (Ravindra Babu et al., 2023).

61 Moreover, extensive open BB in spring over Peninsular Southeast Asia (PSEA), including
62 Myanmar, Thailand, Cambodia, Laos, and Vietnam, serves as a key source of aerosols affecting
63 the SCS atmosphere (Chan et al., 2003; Ou-Yang et al., 2012; Yadav et al., 2017; Liao et al., 2021;
64 Wang et al., 2021; Pani et al., 2023; Wang et al., 2025). This region is recognized as a global
65 hotspot for BB (Lin et al., 2013; Reid et al., 2013; Cohen, 2014; Cohen et al., 2017; Pani et al.,
66 2019), significantly contributing to carbon emissions and aerosol loading during the peak fire
67 season in March and April (Ravindra Babu and Lin, 2023). These fires mainly stem from annual
68 slash-and-burn farming practices across PSEA (Lee et al., 2016; Tsay et al., 2016; Huang et al.,
69 2020), releasing substantial particulate matter and trace gases into the air (Ou-Yang et al., 2022).
70 As a result, aerosol variability in the SCS region is largely driven by interactions between regional
71 emission sources and the prevailing monsoon circulation, which influence aerosol transport,
72 dispersion, and accumulation within the basin (Pani et al., 2023).

73 The year 2023 saw exceptional wildfires worldwide due to record-high global mean surface
74 temperatures, which affected carbon emissions and aerosol levels (Esper et al., 2024; Forster et al.,
75 2024; Min, 2024; Raghuraman et al., 2024; Kolden et al., 2024; Liu et al., 2024; Byrne et al., 2024;
76 MacCarthy et al., 2024). It has been reported that 70% of total burning occurs in the Northern
77 Hemisphere (Kolden et al., 2024). Among all, Canadian wildfires emerged as the primary hotspot,
78 with significant fires in both the eastern and western regions causing notable increases in carbon
79 monoxide (CO) and tropospheric aerosols over the past twenty years (Liu et al., 2024; Byrne et
80 al., 2024; MacCarthy et al., 2024). Although the unprecedented Canadian wildfires in 2023
81 received considerable scientific attention and were well documented in several studies, the record-
82 breaking aerosol loading over the SCS in April 2023 attracted relatively little international
83 attention. The historic event over the SCS in April 2023 can be seen through the Moderate
84 Resolution Imaging Spectroradiometer (MODIS) Aqua AOD anomalies compared to the long-
85 term mean (2003-2022), which shows extreme positive anomalies over the SCS and surrounding
86 regions during that month, contrasting with the rest of the globe (**Fig. 1**). However, AOD
87 anomalies in May illustrate the absence of positive anomalies over the SCS and instead show
88 higher positive anomalies over North America, which are related to the Canadian wildfires. The
89 time series of monthly mean AOD over the SCS further confirms a record-high AOD in April 2023
90 relative to the MODIS data from 2003 to 2023 (**Fig. 2d**). The exceptional aerosol loading in April
91 2023 is unusual for remote marine locations such as the SCS and warrants further investigation.

92 In this study, we investigated the factors and physical processes that contributed to the
93 unprecedented aerosol levels observed in April 2023, using extensive data collected from multiple
94 sources over an extended period. The following three major topics are examined in detail within
95 this study:

- 96 • How extreme are these AOD anomalies, and what magnitude was increased?
- 97 • What are the sources for these record-breaking aerosol loadings over SCS?
- 98 • Were dynamic and large-scale circulations responsible for this event?



99
100 **Figure 1.** MODIS Aqua measured AOD anomalies in (a) April 2023 and (b) May 2023 compared
101 to the long-term mean (2003-2022). The highlighted circles in (a) and (b) indicate the AOD
102 anomalies over the South China Sea (SCS) and Canada regions. This figure highlights that the
103 AOD anomalies observed by MODIS are significant and particularly pronounced over the SCS

104 compared to the other areas globally. It illustrates the unique characteristics of April 2023
105 compared to long-term mean. Data visualizations produced using MATLAB 2023b
106 (<https://matlab.mathworks.com>).

107 **2. Data and Methodology**

108 **2.1 Data**

109 This study relies entirely on publicly available data, covering the period from 2003 to 2023. We
110 used data products from various satellite measurements, ground-based observations, and reanalysis
111 products.

112 **2.1.1 Satellite remote sensing measurements**

113 **Moderate Resolution Imaging Spectroradiometer (MODIS)**

114 MODIS is a passive sensor aboard the Aqua and Terra satellites, which are in sun-synchronous
115 orbits and cross the Equator in the morning (Aqua) and afternoon (Terra). From MODIS satellite
116 measurements, we utilized aerosol optical depth (AOD), fire counts, fire radiative power (FRP),
117 cloud fraction, and burned area products. We used Level 3 monthly AOD at $1^\circ \times 1^\circ$ spatial
118 resolution derived from the mean of the Dark Target and Deep Blue Combined Aerosol Products
119 from the Terra satellite (MOD08_M3 Collection 6.1) and Aqua satellite (MYD08_M3 Collection
120 6.1) (Platnick et al., 2015; Buchholz et al., 2020). For MODIS AOD, the estimated uncertainty is
121 approximately ± 0.05 over ocean and ± 0.15 over land. The Collection 6.1 (C6.1) products used in
122 this study have been shown to capture temporal variations effectively and agree closely with
123 ground-based observations (Wei et al., 2019a). Validation against AErosol RObotic NETwork
124 (AERONET) measurements demonstrates that the merged Dark Target and Deep Blue (DTB)
125 products accurately capture aerosol variability at both regional and global scales (Sayer et al.,
126 2014; Wei et al., 2019b). Additionally, we used MODIS's daily fire counts and fire radiative power
127 (FRP) products (Giglio et al., 2006, 2016, 2018). Direct fire counts from MODIS were obtained
128 from the Fire Information for Resource Management System (FIRMS) dataset. We selected all
129 MODIS fire counts from the Terra and Aqua sensors with a confidence level of at least 80%.
130 Finally, we utilized Cloud Fraction data from both the Terra and Aqua satellites.

131 **Measurements Of Pollution In The Troposphere (MOPITT)**

132 MOPITT is a multi-channel thermal infrared (TIR) and near-infrared (NIR) instrument operating
133 on board the sun-synchronous polar-orbiting NASA Terra satellite. This study uses a version 9
134 (MOP03TM_9) gridded monthly product (Worden et al., 2010; Deeter et al., 2019). For more
135 details on the retrieval algorithm, validation, and uncertainties in MOPITT CO, see Deeter et al.
136 (2019).

137 **Atmospheric Infrared Sounder (AIRS)**

138 In addition to the MOPITT measurements, we used CO from the AIRS instrument on the NASA
139 Aqua satellite, which provides CO at multiple vertical levels twice daily and has near-global
140 coverage. AIRS uses wavenumbers 2183–2200 cm⁻¹ (4.58–4.5 μm) for retrieving CO (McMillan
141 et al., 2005). The V9 level 3 CO product, available at 1° × 1° resolution at 700 and 500 hPa levels,
142 was utilized in the present study. AIRS sensitivity to CO is broad and optimal in the mid-
143 troposphere between approximately 300 and 600 hPa (Warner et al., 2007, 2013; AIRS project,
144 2019). CO retrievals exhibit a 6%–10 % bias between 900 and 300 hPa with a root mean square
145 error of 8%–12 % (McMillan et al., 2011). In addition to CO, we also utilized, surface temperature,
146 and outgoing longwave radiation (OLR) data from the AIRS satellite.

147 **Global Precipitation Climatology Project (GPCP)**

148 The Global Precipitation Climatology Project (GPCP) Version 3.2 Satellite-Gauge (SG)
149 Combined Precipitation Data Set was used during the study period. The data is available for
150 download from <https://measures.gesdisc.eosdis.nasa.gov/data/GPCP/GPCPMON.3.2/> (last
151 accessed June 5, 2025).

152 **Cloud-Aerosol LIDAR with Orthogonal Polarization (CALIOP)**

153 The CALIOP sensor on the Cloud-Aerosol Lidar and Infrared Pathfinder Satellite Observations
154 (CALIPSO) satellite provides data on atmospheric aerosols, including aerosol layer heights and
155 thicknesses, optical depth, aerosol type, and other optical properties (Omar et al., 2009; Kim et al.,
156 2018). In our study, we used vertical aerosol-type images available on the CALIPSO website.

157 **2.1.2 Reanalysis/model products**

158 **MERRA-2 reanalysis**

159 We used monthly mean geopotential height, wind vectors (zonal and meridional wind speeds),
160 and, total column black carbon, organic carbon, and particulate matter from the Modern-Era
161 Retrospective Analysis for Research and Applications, version 2 (MERRA-2). MERRA-2 is the
162 latest atmospheric reanalysis data produced by the NASA Global Modeling and Assimilation
163 Office (GMAO; Gelaro et al., 2017). The horizontal resolution of the MERRA-2 reanalysis is 0.5°
164 $\times 0.625^\circ$.

165 **Global Land Data Assimilation System (GLDAS)**

166 Monthly mean soil moisture content (10 - 40 cm underground) from the Global Land Data
167 Assimilation System (GLDAS)_NOAH025_M v2.1 is utilized. The data can be downloaded from
168 https://hydro1.gesdisc.eosdis.nasa.gov/data/GLDAS/GLDAS_NOAH025_M.2.1/ (last accessed:
169 June 05, 2025).

170 **2.1.3 Ground-based observations**

171 **AERONET**

172 In this study, we use the latest version (V3) of Level 2.0 AERONET data from two stations:
173 Dongsha Island (also called the Pratas Islands; Dongsha_Island, 20.70°N , 116.73°E , 5 m above
174 sea level) and Lulin Atmospheric Background Station (LABS, $23^\circ28'\text{N}$, $120^\circ52'\text{E}$, 2,862 m; Sheu
175 et al., 2010). These offer cloud-screened, quality-checked direct-sun AOD retrievals with
176 uncertainties of about ± 0.01 in the visible and ± 0.02 in the ultraviolet range (Giles et al., 2019;
177 Sinyuk et al., 2020).

178 The summary of the major data used in the present study is presented in **Table 1**.

179 **Table 1.** Details of various data products used in the present study.

Data	Resolution	Source
Aerosol Optical Depth (AOD)	$1^\circ \times 1^\circ$	Aqua and Terra satellite/MODIS
Carbon Monoxide (CO)	$1^\circ \times 1^\circ$	MOPITT and AIRS

Burned Area (BA)	500 m	Aqua and Terra satellite/MODIS
MODIS Collection 6.1 Fire Anomalies		combined Terra and Aqua satellite/MODIS
Wind and Geopotential Height	$0.5^{\circ} \times 0.625^{\circ}$	MERRA reanalysis

180

181 **2.2 Methodology**

182 The anomalies in the various parameters for April 2023 were estimated by subtracting the April
 183 background long-term mea (2003-2022) from April 2023 value.

184 The magnitude of the AOD/CO enhancement in April 2023 above the long-term background was
 185 determined by comparing the average of April 2003-2022. We obtained the percentage change in
 186 AOD/CO relative to the respective background using Equation 1:

187
$$\text{Relative change in percentage} = \left(\frac{x_i - \bar{x}}{\bar{x}} \right) \times 100 \quad (\text{Eq. 1})$$

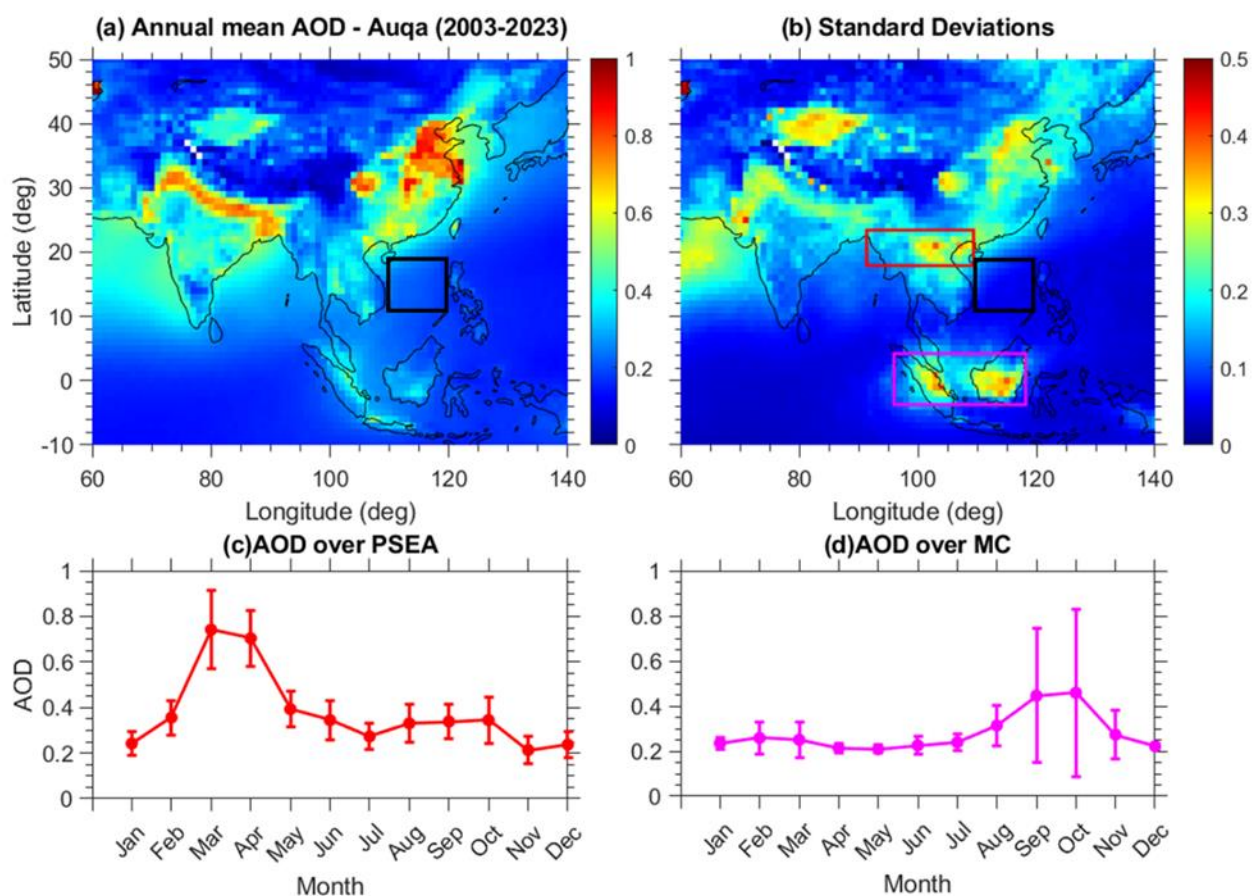
188 where x_i represents the monthly mean of April in 2023, and \bar{x} is the long-term mean of April
 189 calculated using the data from 2003 to 2022.

190 **3. Results and Discussion**

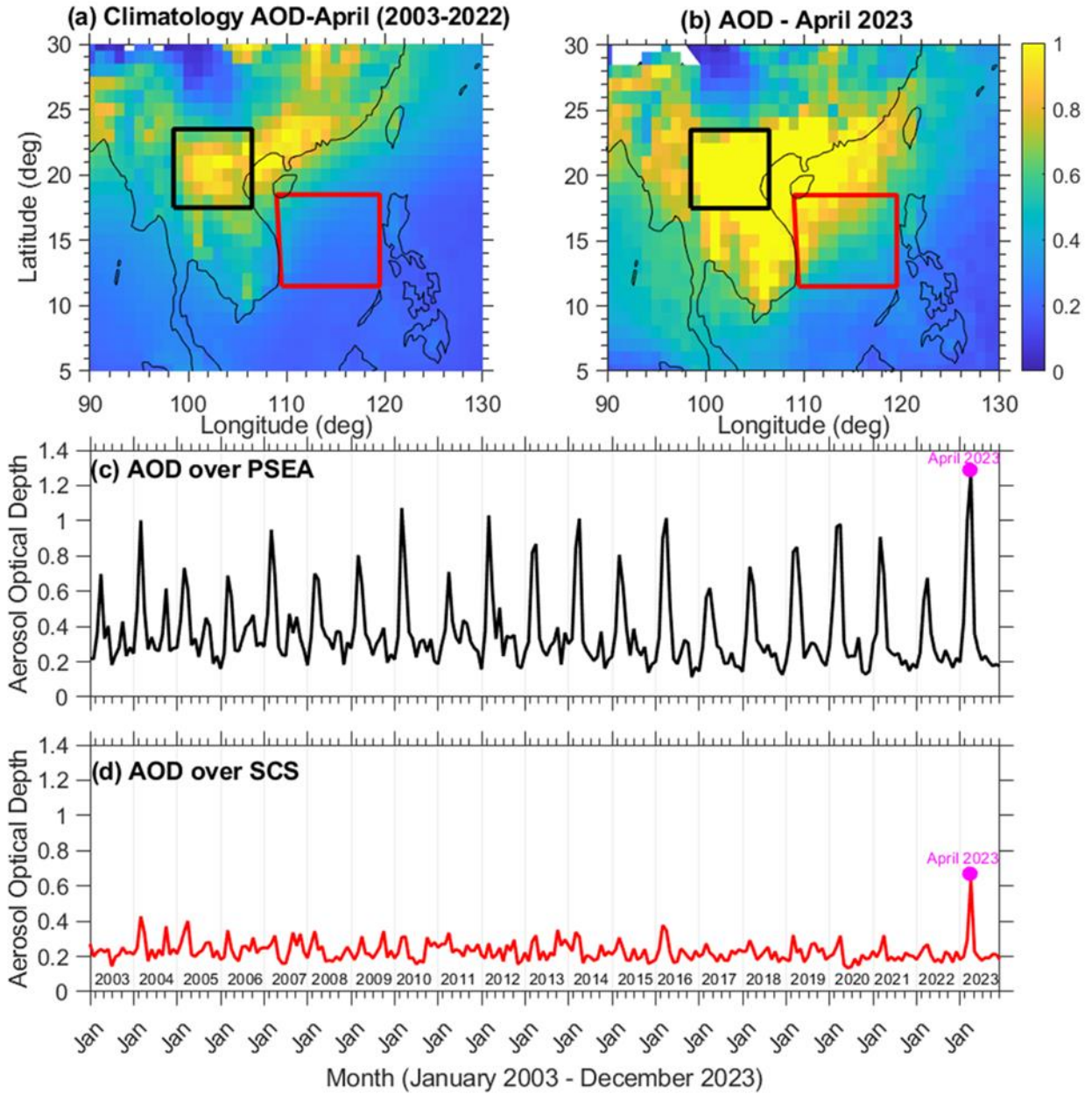
191 **3.1 Record-breaking aerosol loading over SCS in April 2023**

192 Aerosol optical depth (AOD) is a common metric for measuring atmospheric aerosol loading and
 193 is crucial for radiative forcing assessments (Hirsch and Koren, 2021). In this study, we use AOD
 194 data from the MODIS instruments aboard the Aqua and Terra satellites for the period. Before
 195 analyzing the unusual AOD conditions observed in April 2023, we first characterize the long-term
 196 AOD behavior over the study area using two decades of MODIS data. The spatial patterns of the
 197 long-term annual mean AOD and its associated standard deviation across the Asian region are
 198 shown in **Figures 2a** and **2b**, respectively. Additionally, the long-term monthly-mean variability
 199 of AOD over the two main BB regions surrounding the SCS, namely PSEA and the MC, is shown

200 in **Figures 2c** and **2d**. The relatively low AOD levels and small standard deviations over the SCS
 201 suggest a predominantly clean marine environment. The seasonal cycle of AOD shows clear peaks
 202 linked to regional BB activities (**Figs. 2c** and **2d**). Over PSEA, AOD peaks during March–April,
 203 while over the MC, the peak occurs in September–October. These seasonal maxima align with
 204 well-known BB activity periods in these areas (Ravindra Babu and Lin, 2024; Chang et al., 2024).
 205 The fire season over the MC usually runs from August to October, whereas PSEA experiences
 206 intense BB activity from January to April, with a notable peak in March.



207
 208 **Figure 2.** Climatological mean distribution of MODIS (a) Aerosol Optical Depth (AOD) and (b)
 209 respective standard deviations. The black box illustrated in both figures emphasizes the specific
 210 area of the South China Sea (SCS) that is the primary focus of this research. (11-18°N,109-119°E).
 211 The red and magenta boxes indicate the PSEA and MC, two significant biomass-burning regions
 212 near the SCS. The long-term average seasonal variation in AOD is illustrated over (c) PSEA and
 213 (d) MC.

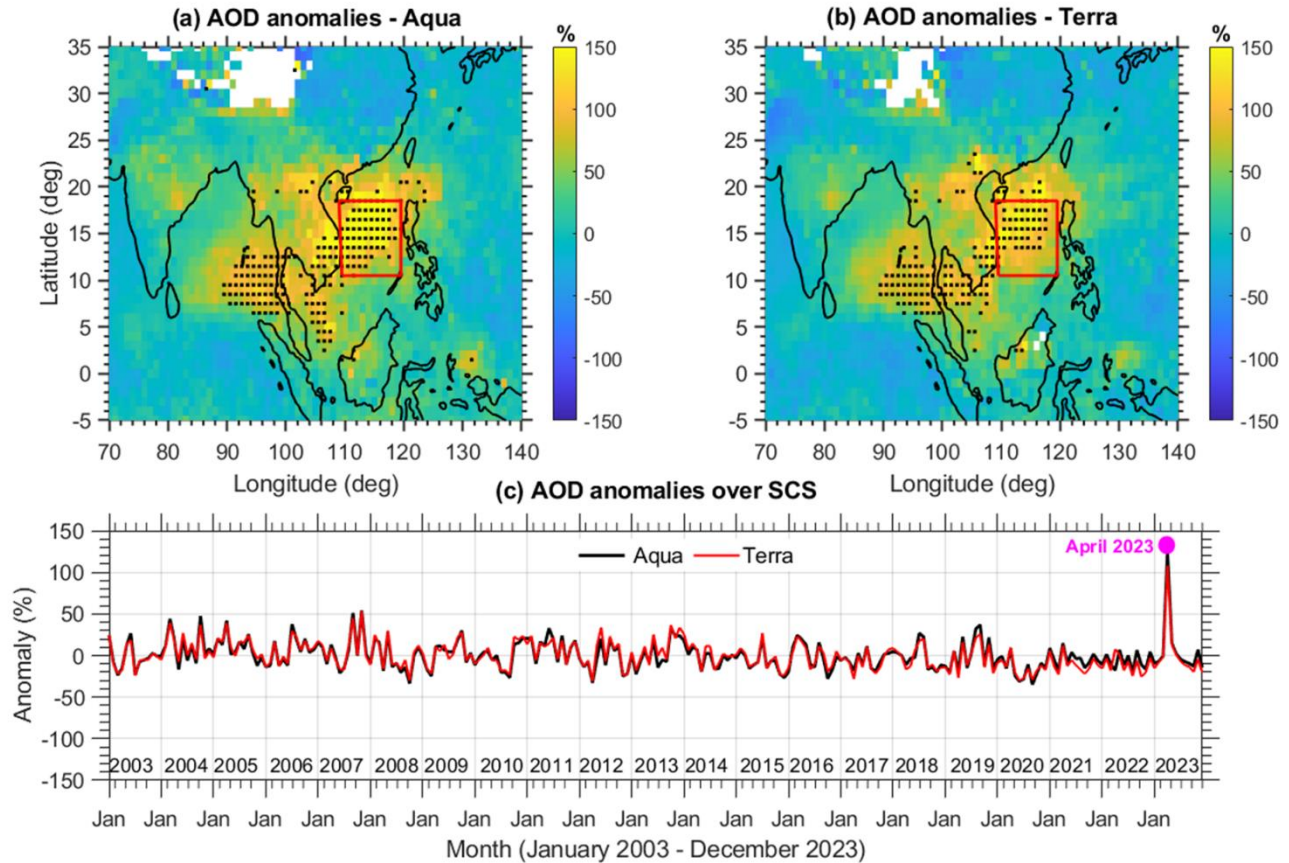


214

215 **Figure 3.** Spatial distribution of (a) Inter-annual (2003 to 2022) monthly average AOD values for
 216 April. (b) Monthly AOD values for April 2023. A notable increase in AOD values is observed
 217 over the Peninsular Southeast Asia (PSEA) and the South China Sea (SCS). AOD distribution
 218 averaged in April over the past two decades showed a belt of high aerosol loading extending from
 219 northern Laos to the southern coast of China. During April 2023, extreme AOD values were
 220 observed across the entire PSEA, extending to coastal South China and the SCS. (c) Time series
 221 of average monthly mean AOD values over the northern PSEA (17-23°N, 99- 106°E), and (d) over
 222 the SCS (11-18°N,109-119°E) from January 2003 to December 2023. The magenta dot in subplots
 223 (c) and (d) marks the AOD values during April 2023.

224 To emphasize the anomalous conditions in April 2023, we present the spatial distribution of April
225 AOD over the study region for both the long-term average and April 2023. The long-term average
226 April AOD for 2003–2022 and the corresponding April 2023 AOD distribution are shown in
227 **Figures 3a** and **3b**. Moreover, the time series of monthly mean AOD from 2003 to 2023 over
228 northern PSEA (17–23°N, 99–106°E) and the SCS (11–18°N, 109–119°E) are displayed in
229 **Figures 3c** and **3d**. The AOD distribution in April over two decades indicates high aerosol loading
230 from northern Laos to coastal South China (15–25°N, 100–120°E). In April 2023, extreme AOD
231 values extended from PSEA to South China and SCS, with the highest values centered between
232 northern Laos and the SCS. Record-breaking AOD levels were observed for the area averaged
233 over the SCS in April 2023, showing a nominal increase in northern PSEA (**Fig. 3c**). However,
234 the highest AOD value for northern PSEA in April 2023 correlates with record AOD over the SCS.
235 Long-term monthly mean AOD from Aqua and Terra (2003–2023) exhibited a strong correlation
236 of 0.97, confirming the consistency and reliability of these observations (**Fig. S1a** in the
237 Supplement). To assess the magnitude of the increase, we estimated the percentage change in AOD
238 by comparing April 2023 with the long-term April average from 2003 to 2022.

239



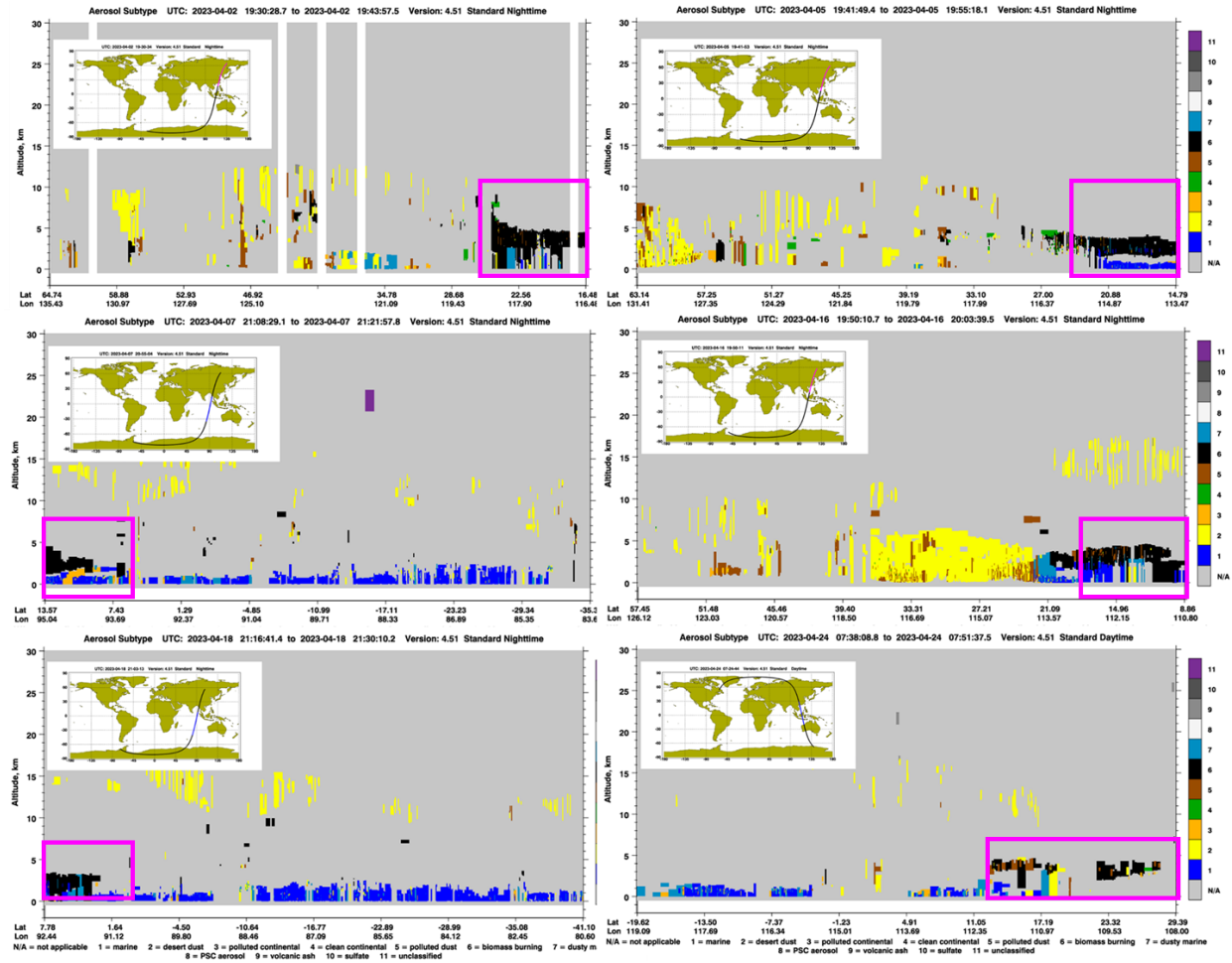
240

241 **Figure 4.** Spatial distribution of the change (%) in Aerosol Optical Depth (AOD) values during
 242 April 2023 compared with the inter-annual April average (2003-2022). (a) AOD anomalies are
 243 obtained from the MODIS Aqua and (b) from the MODIS Terra satellite. The black dots indicate
 244 that the anomalies exceed 4σ of the long-term mean. (c) Time series of area-averaged AOD
 245 anomalies expressed in percentage change over the South China Sea (SCS) domain from the Aqua
 246 (black line) and Terra (red line) satellites. The most pronounced enhancement occurred over the
 247 SCS, where April AOD anomalies exceeded 4σ above the long-term mean.

248 **Figures 4a** and **4b** illustrate the spatial extent of AOD anomalies, shown as percentage
 249 changes, based on data from MODIS Aqua and Terra satellites. In April 2023, there was a
 250 widespread and unexpected increase of about 150% across most of the SCS and southern Bay of
 251 Bengal (BoB), with anomalies surpassing roughly 4 standard deviations. The area-averaged AOD
 252 anomalies (%) over the SCS, indicated by the black line for Aqua and the red line for Terra, reveal
 253 that the April 2023 peak was the highest on record compared to data from 2003 to 2023,
 254 emphasizing the extreme AOD intensity that month. These satellite observations were also
 255 supported by ground-based measurements from AERONET. The only operational AERONET
 256 remote station downwind of PSEA BB, with over a decade of continuous AOD measurements

257 (Fig. S2a in the Supplement), within the SCS region, is located on Dongsha Island (also known as
258 Pratas Island, 20.70°N, 116.73°E; 5 m a.s.l.). Analysis of monthly mean AOD data from Dongsha
259 Island indicates that April 2023 had the highest AOD value during the observational period from
260 January 2009 to December 2023 (Fig. S2c in the Supplement). AERONET comparisons show
261 strong correlations with MODIS AOD: 0.86 for Aqua and 0.87 for Terra (Fig. S3 in the
262 Supplement), supporting the reliability of the satellite observations. Because AOD is a column-
263 integrated measure, it does not provide information on the vertical distribution of aerosols. To
264 address this limitation, we further analyzed vertical distribution images of aerosols from the Cloud-
265 Aerosol Lidar and Infrared Pathfinder Satellite Observation (CALIPSO), which reveal pronounced
266 enhancements in smoke aerosol over the SCS (Fig. 5). Elevated smoke layers were also observed
267 over the southern BoB in April 2023, predominantly within the mid-troposphere at altitudes of
268 approximately 2-5 km. Consistent with these CALIPSO lidar observations, MERRA-2 reanalysis
269 data indicate substantial increases in aerosol mass concentrations in 2023, with black carbon (BC)
270 increasing by ~250% and organic carbon (OC) by ~350% (Fig. S4 in the Supplement). The most
271 pronounced enhancements occur between 700 and 600 hPa, closely matching the altitude range
272 identified by CALIPSO. The concurrence of satellite (MODIS and CALIPSO) and reanalysis data
273 points to a severe pollution episode in April 2023 over and surrounding regions of the SCS,
274 characterized by an elevated aerosol layer indicative of long-range-transported BB smoke.
275 Notably, the SCS is a relatively clean remote marine region with limited local aerosol sources. In
276 such environments, enhanced aerosol loading is typically associated with long-range transport of
277 pollutants from surrounding continental regions (Pani, 2023). Given the potential influence of
278 long-range transport of pollutants, we further analyzed variations in carbon monoxide (CO), a
279 widely used tracer of BB emissions due to its relatively long atmospheric lifetime (~1–2 months)
280 and strong association with incomplete combustion (Ravindra Babu et al., 2023). We investigated
281 CO changes across the study region using measurements from the MOPITT and AIRS satellites,
282 which together provide more than two decades of continuous CO observations. CO data at 700
283 and 500 hPa from both satellites were analyzed for the period 2003–2023, with the 500 hPa level
284 representing the altitude of maximum sensitivity for CO retrievals (Buchholz et al., 2021).

285

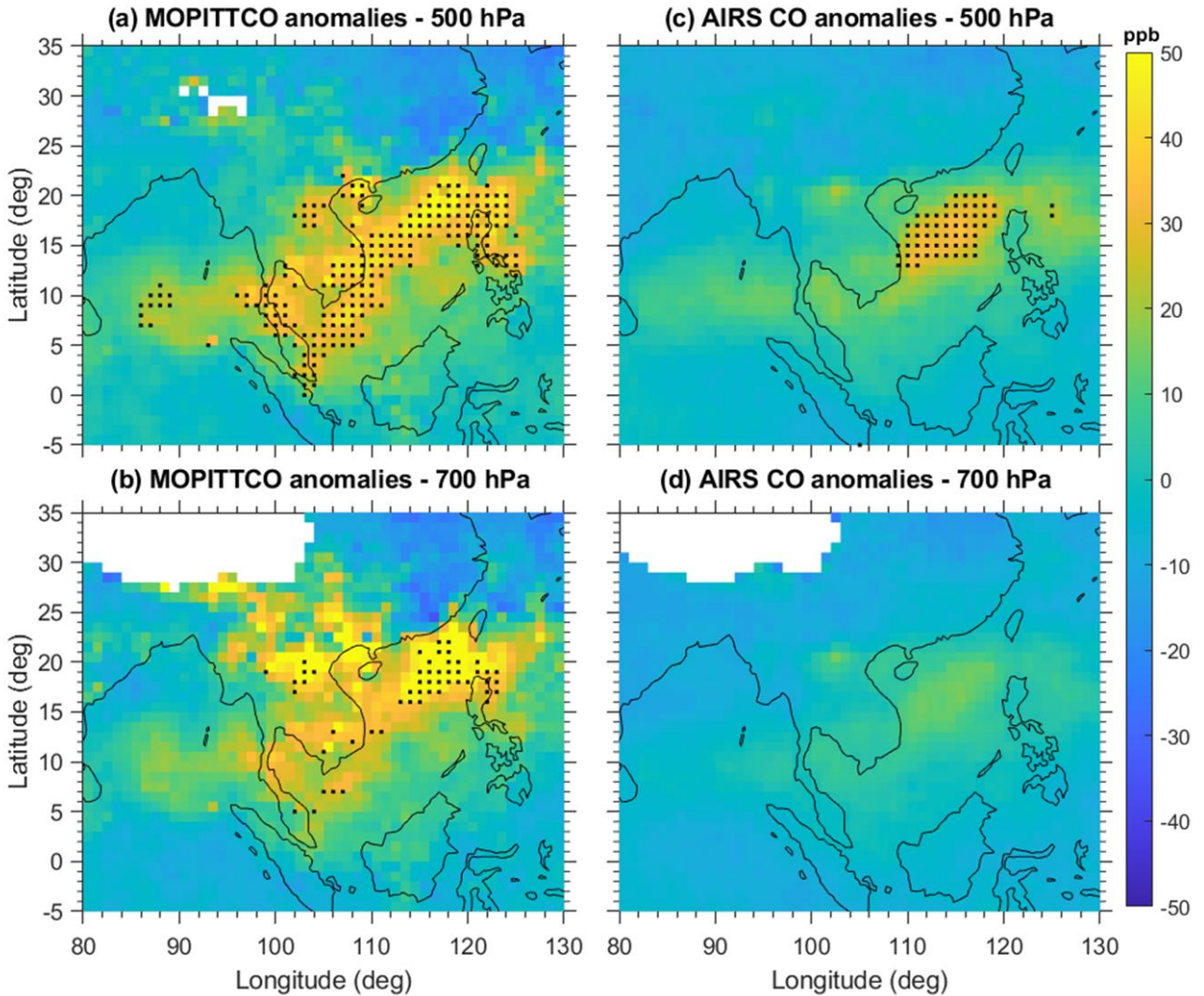


286

287 **Figure 5.** Aerosol subtype images obtained by the CALIPSO observations during various days in
 288 April 2023. The highlighted magenta box indicates elevated smoke over the South China Sea
 289 (SCS) and the southern Bay of Bengal. Smoke aerosol is shown in black.

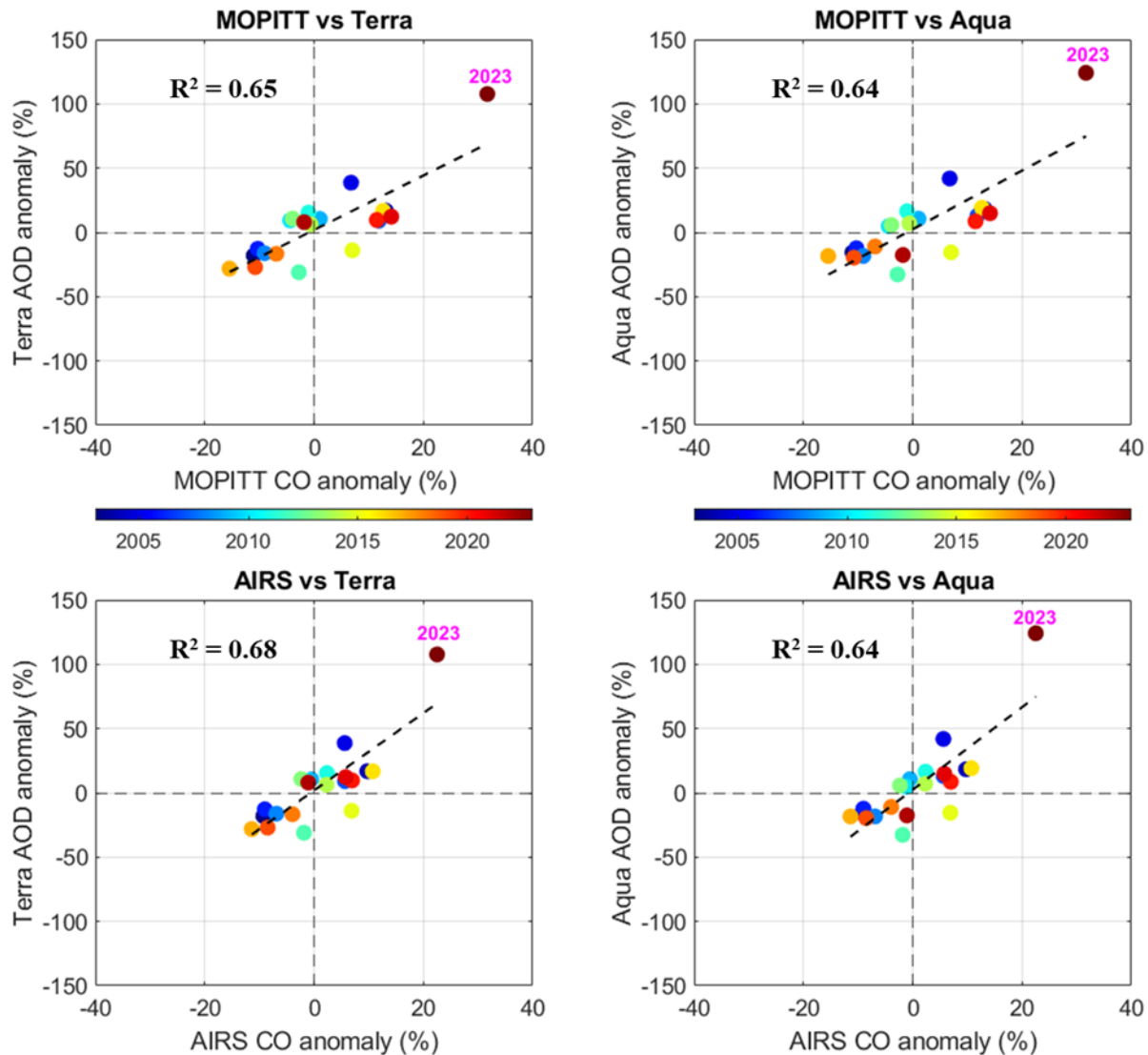
290 The observed CO anomalies from the two satellites are shown in **Fig. 6**, revealing
 291 significantly elevated CO concentrations over the SCS in April 2023, reaching up to 3σ above the
 292 2003–2022 climatology. Although MOPITT displays more spatially concentrated anomalies than
 293 AIRS, both datasets consistently show positive CO anomalies at both pressure levels, indicating a
 294 substantial increase in mid-tropospheric CO during this period. For MOPITT CO retrievals,
 295 primary sources of uncertainty include limitations in vertical sensitivity and potential retrieval
 296 biases (Sayer et al., 2014; Wei et al., 2019). However, the observed enhancements ($>3\sigma$) are
 297 supported by independent AIRS CO measurements, reinforcing the robustness of the detected
 298 anomalies. The comparison between MOPITT and AIRS CO at 500 hPa over the SCS further
 299 shows a strong positive correlation ($R \approx 0.89$; **Fig. S1b** in the Supplement). Furthermore, the

300 spatial distribution of CO anomalies closely resembles that of AOD anomalies (**Fig. 4**). The area-
301 averaged anomalies of AOD and 500 hPa CO over the SCS in April during 2003-2023 exhibit a
302 strong positive correlation ($R = 0.81$; **Fig. 7**), suggesting that long-range transport of pollution
303 plays an important role in modulating aerosol variability in this region. The bubble chart further
304 highlights the exceptional severity of the April 2023 event compared with previous years (**Fig. 7**).
305 Because CO is primarily produced by incomplete combustion, elevated concentrations far from
306 major traffic or industrial sources strongly suggest BB and wildfire emissions. The strong
307 similarity between the spatial distributions of CO and AOD anomalies suggests that the increased
308 aerosol loading was driven by BB in April 2023. This indicates that smoke was likely transported
309 from surrounding regions toward the SCS and the BoB, which are located near major BB hotspots,
310 including the MC and PSEA. The MC fire season typically occurs from August to October,
311 whereas PSEA experiences a BB season from January to April, peaking in March (**Fig. 2**). These
312 seasonal characteristics strongly suggest that the elevated AOD levels observed over the SCS in
313 April 2023 were likely linked to BB activity in PSEA. Overall, the April 2023 event is notable for
314 its exceptional intensity and extensive spatial coverage. The MODIS AOD anomalies were
315 approximately four times higher than the long-term mean across much of the SCS and the southern
316 BoB during April 2023. Such anomalously high aerosol loading over the SCS may have important
317 implications for the regional climate and the hydrological cycle, highlighting the need for further
318 investigation into the underlying drivers and physical mechanisms responsible for this event.



319

320 **Figure 6.** Spatial distribution of carbon monoxide (CO) anomalies in April 2023 at (a) 500 hPa
 321 and (b) 700 hPa from MOPITT satellite measurements. Panels (c) and (d) show the corresponding
 322 CO anomalies at 500 hPa and 700 hPa derived from AIRS satellite observations. Anomalies are
 323 calculated relative to the long-term April mean for 2003–2022. Black dots indicate regions where
 324 anomalies exceed the 3σ significance threshold.



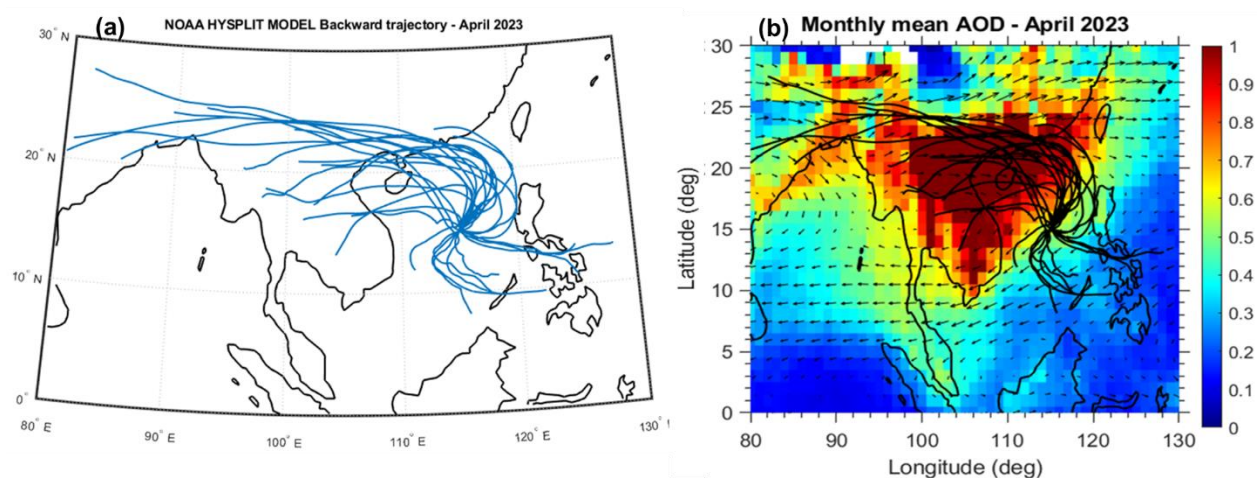
325

326 **Figure 7.** Bubble plot of the AOD and CO anomalies (April) over the South China Sea (SCS)
 327 during 2003–2023. Top panels for MOPITT and MODIS (Terra and Aqua), whereas the bottom
 328 panels are for AIRS and MODIS observations. The average coefficient of determination (R^2) is
 329 ~ 0.65 , corresponding to a correlation coefficient (R) of 0.81, indicating a statistically robust
 330 association between CO and AOD over the SCS.

331 3.2 Transport and Source Attribution of the April 2023 Aerosol Event

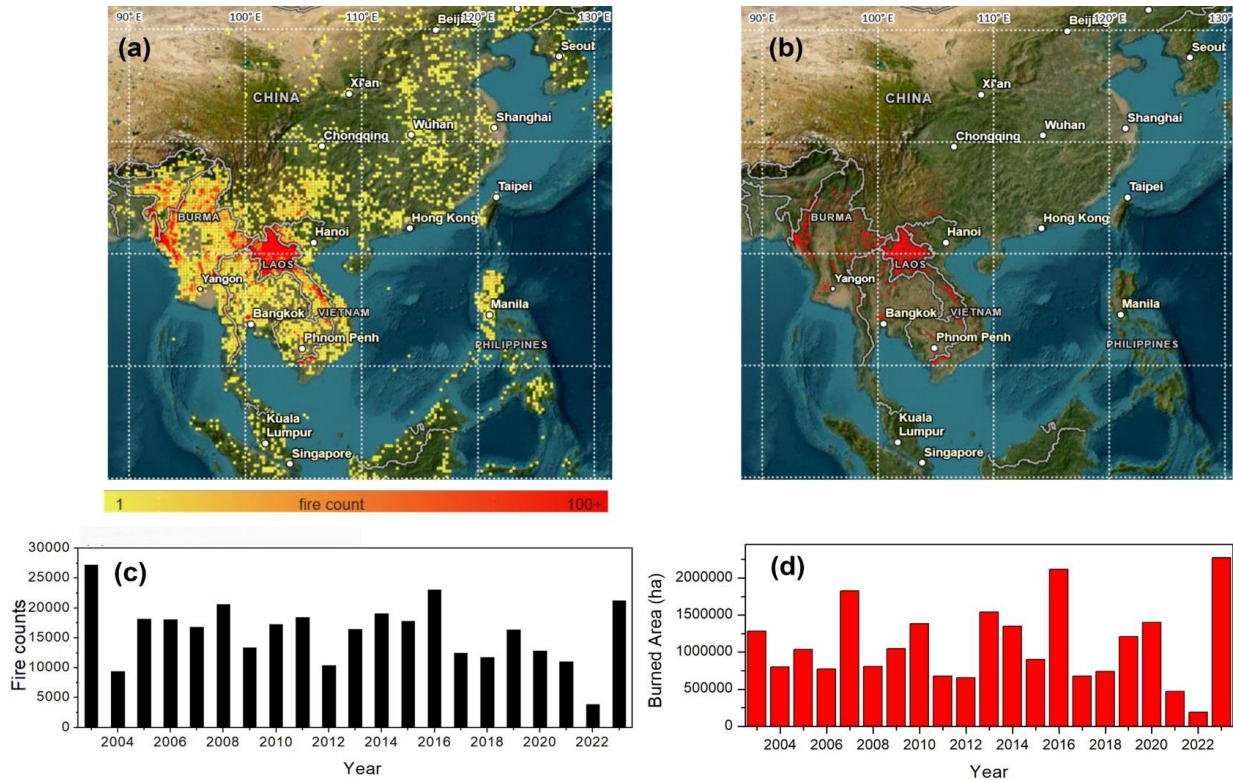
332 From the previous section, it is clear that most aerosols are free-troposphere-dominated
 333 and located primarily in the ~ 2 -5km region over the SCS. To determine the source regions
 334 responsible for elevated aerosol concentrations over the SCS in April 2023, backward air-mass
 335 trajectories were computed using the NOAA HYSPLIT model. Trajectories were initialized at
 336 15°N , 115°E , at 3 km above sea level, corresponding to the altitude range (2-5 km) of the elevated

337 aerosol layer observed in CALIPSO and MERRA-2 profiles. Daily 72-hour trajectories (**Fig. 8a**)
 338 indicate that air masses arriving over the SCS predominantly originated from northern PSEA.
 339 When overlaid on the monthly mean MODIS AOD (**Fig. 8b**), these trajectories reveal transport
 340 pathways that coincide with regions of high aerosol loading, strongly suggesting that long-range
 341 transport of PSEA BB smoke likely transported to the SCS. To examine the BB activity during
 342 April 2023, MODIS fire counts and burned area (BA) data were used. The spatial distributions of
 343 MODIS fire counts and BA for April 2023 (**Figs. 9a–b**) show that BB activity was overwhelmingly
 344 concentrated in northern PSEA, particularly in northern Laos and adjacent regions of Myanmar
 345 and Thailand. Minimal fire activity and BA were observed over the MC and southern China;
 346 therefore, these regions were excluded from source-region calculations. Analysis of inter-annual
 347 variability in April BB activity over PSEA from 2003 to 2023 (**Figs. 9c–d**), considering only fire
 348 detections above the 80% confidence level, indicates substantial year-to-year fluctuations.
 349 Notably, April 2023 recorded the highest burned area (~2.27 Mha) over the 21-year period,
 350 highlighting the exceptional intensity of BB activity that month.



351
 352 **Figure 8.** (a) Daily 72-h NOAA HYSPLIT backward trajectories ending at 12:00 UTC at a
 353 representative location (15°N, 115°E) over the South China Sea (SCS) at 3 km altitude for April
 354 2023. (b) Same as (a), but overlaid on the monthly mean MODIS aerosol optical depth (AOD) for
 355 April 2023.

356



357

358 **Figure 9.** Spatial distribution of the (a) MODIS fire counts, (b) MODIS Global Burned Area
 359 Product in April 2023. Inter-annual variability in (c) Fire counts, and (d) Burned Area over
 360 Peninsula Southeast Asia in April from 2003 to 2023. (Source:
 361 <https://firms.modaps.eosdis.nasa.gov/>). For inter-annual variability in fire counts, we considered
 362 those above the 80% confidence level.

363 Country-level statistics (**Table 2**) further highlight the dominant contribution from Laos,
 364 which accounted for 11,877 fires (56.0%), 1.53×10^6 MW of fire radiative power (FRP; 63.5%),
 365 and 1.08×10^6 ha of burned area (47.7%). Notably, the BA observed in April 2023 represents the
 366 highest monthly value in the available dataset (2002–2023; **Fig. S5** in the Supplement).
 367 Approximately 60% of Laos is forested (**Fig. S6** in the Supplement), with much of this forest
 368 located in northern Laos where the majority of fires occurred during April 2023 (**Fig. 9a**).
 369 Myanmar contributed the second-largest share, with 7,054 fires (33.3%), 7.78×10^5 MW of FRP
 370 (32.3%), and 9.15×10^5 ha of burned area (40.3%). Thailand, Vietnam, and Cambodia contributed
 371 comparatively smaller burned areas of 1.21×10^5 ha, 1.30×10^5 ha, and 2.20×10^4 ha, respectively.
 372 In total, 21,198 fires across PSEA produced approximately 2.41×10^6 MW of FRP in April 2023.
 373 These results strongly suggest that intense BB activity over northern PSEA, likely contributed
 374 substantially to the exceptional aerosol loading observed over the SCS in April 2023. However,
 375 two key questions remain: (i) what factors triggered the anomalously strong fire activity in Laos

376 during April 2023, and (ii) why were BB aerosols transported unusually far southward across the
 377 SCS and into the southern BoB, rather than following the more typical transport pathways toward
 378 Taiwan and the north western Pacific? To address these questions, we next examine the large-scale
 379 meteorological and dynamical circulation conditions prevailing during April 2023.

380 **Table 2.** MODIS total fire counts, the corresponding total accumulated fire radiative power (FRP),
 381 and the burned area (BA) observed over peninsular Southeast Asia (PSEA) and each country
 382 within PSEA in April 2023. The percentage contribution of each country to the total number of
 383 fires, the total FRP, and the BA of PSEA is shown in brackets.

Country	Total Fires	Fire Radiative Power (MW)	Burned Area (ha)
PSEA	21198	2407283	2272099.89
Country	Total Fires	FRP	BA
Cambodia	242 (1.14%)	13402 (0.5%)	21959.5 (0.97%)
Laos	11877 (56.02%)	1530000 (63.5%)	1084050 (47.71%)
Myanmar	7054 (33.27%)	777970 (32.32%)	915175.7 (40.27%)
Thailand	1322 (6.24%)	50276 (2.1%)	120573.7 (5.31%)
Vietnam	703 (3.32%)	35634 (1.5%)	130340.7 (5.74%)

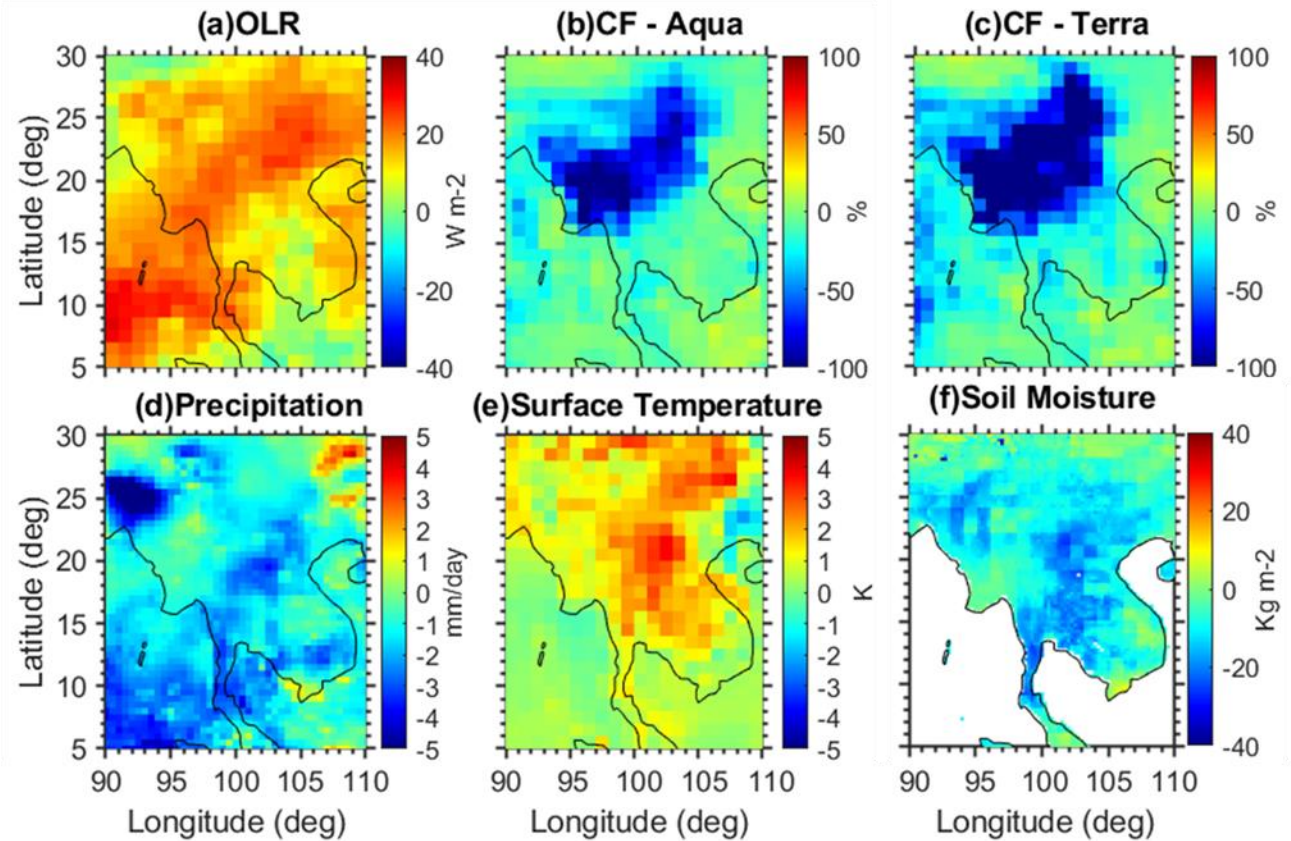
384

385 3.3 Large-scale meteorological and dynamical circulation anomalies in April 2023

386 In this section, we examine the meteorological and large-scale dynamical circulation
 387 anomalies associated with the April 2023 event. **Figure 10** presents the spatial distribution of
 388 anomalies in key meteorological parameters during April 2023 relative to the 2003–2022
 389 climatological mean. As shown in **Figure 10**, Outgoing Longwave Radiation (OLR) anomalies
 390 indicate suppressed convective activity over PSEA during April 2023. Reduced convection was
 391 accompanied by negative precipitation anomalies, elevated surface temperatures, and pronounced
 392 soil moisture (SM) deficits. These conditions are spatially consistent with the regions of enhanced
 393 fire counts and BA observed by MODIS over northern Laos (**Fig. 9**). Long-term SM anomalies
 394 over northern Laos reached exceptionally low values in April 2023, representing the lowest levels

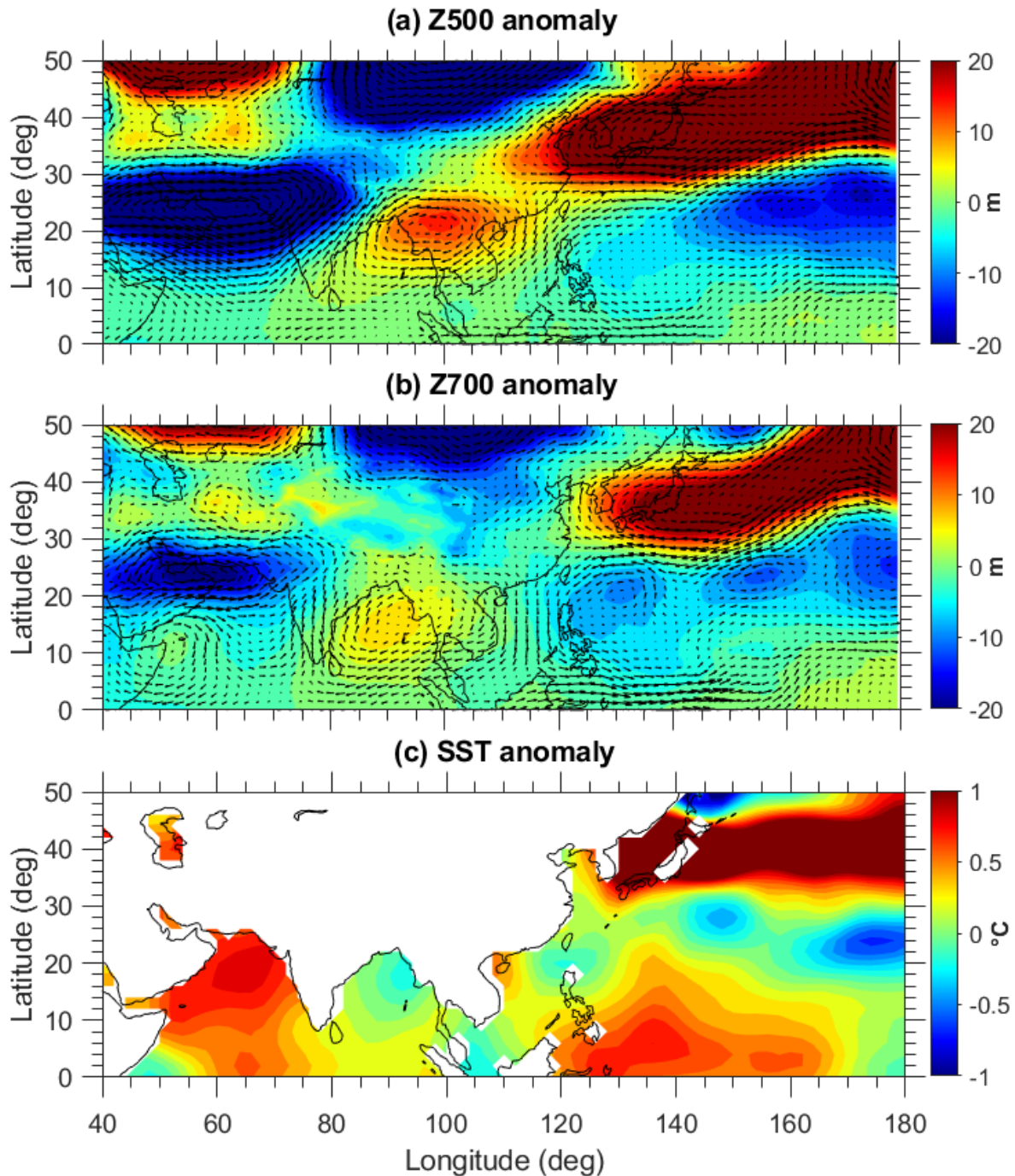
395 in the past two decades (**Figs. S7a–b** in the Supplement). To further examine the persistence of
396 these conditions, we analyzed the temporal evolution of SM anomalies during 2021–2023. The
397 results show maximum positive anomalies in March 2022 and a transition to strong negative
398 anomalies by April 2023, indicating a prolonged drought from winter 2022 to April 2023 (**Fig.**
399 **S7c** in the Supplement). We further assessed the relationship between SM anomalies and fire
400 activity over Laos. Standardized fire anomalies and SM anomalies (**Fig. S8** in the Supplement)
401 reveal a significant inverse relationship: reduced SM is associated with enhanced fire activity. In
402 April 2023, extreme negative SM anomalies coincided with strong positive fire anomalies,
403 highlighting the role of severe surface drying in promoting intense BB activity. A similar co-
404 occurrence of anomalously low SM and elevated fire activity is also evident in 2016, a year
405 previously identified as having intensified regional burning. These findings provide additional
406 observational evidence that SM deficits are linked to enhanced fire activity over PSEA. Previous
407 studies have shown that negative SM anomalies can promote positive geopotential height
408 anomalies in the upper troposphere, which tend to reinforce local high-pressure conditions and
409 enhance surface warming (e.g., Fischer et al., 2007; Dong et al., 2023). Motivated by this
410 mechanism, we next examine the large-scale dynamical circulation patterns during April 2023 to
411 understand how atmospheric dynamics may have contributed to the observed meteorological
412 anomalies and the anomalous transport of BB aerosols.

413



414

415 **Figure 10.** Surface and atmosphere conditions in April 2023. April anomalies in 2023 compared
 416 to the 2003-2022 climatological period for (a) Outgoing Longwave radiation (OLR), (b) cloud
 417 fraction (CF) from Aqua, (c) cloud fraction from Terra, (d) precipitation, (e) Surface Temperature,
 418 (f) soil moisture (10 - 40 cm underground). OLR and surface temperatures are obtained from AIRS
 419 satellite measurements. CF data from MODIS Aqua and Terra. Soil moisture is obtained from the
 420 GLDAS Noah Land Surface Model L4 monthly 0.25 x 0.25 degree V2.1. Precipitation data is
 421 obtained from the Global Precipitation Climatology Project (GPCP) Version 3.2.



422

423 **Figure 11.** Spatial distribution of (a) 500 hPa geopotential height (Z500), (b) 700 hPa geopotential
 424 height (Z700), and (c) Sea Surface Temperature (SST) anomalies in April 2023. The anomalies
 425 are calculated by subtracting the April 2023 monthly mean from the April climatology for the
 426 period 1991 to 2020. The wind anomalies for the respective pressure levels are overlaid in Z500
 427 and Z700 anomalies. The geopotential height and wind data are from the MERRA-2 reanalysis,
 428 while SST data are from the NOAA Extended Reconstructed SST V5.

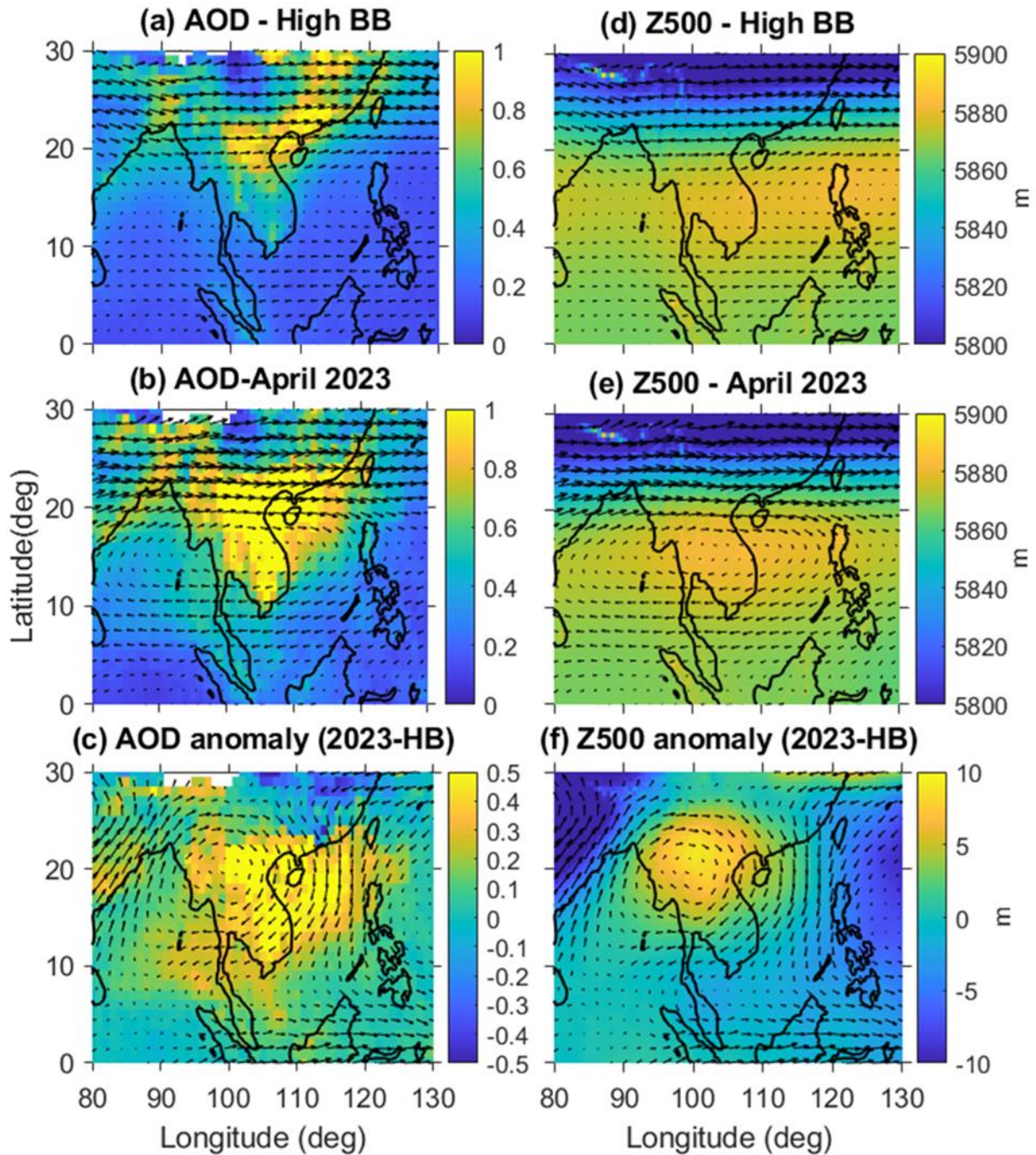
429

430 Our analysis focuses on geopotential height and horizontal wind fields at the 700- and 500-
431 hPa levels. The geopotential height fields (Z700 and Z500) in April 2023 show clear departures
432 from the April climatology (1991–2020) (**Figs. S9–10** in the Supplement). At 700 hPa, the
433 climatological high-pressure system over the Indian region extended eastward toward PSEA, while
434 at 500 hPa, the western Pacific subtropical anticyclone shifted westward to lie directly over PSEA.
435 Geopotential height anomalies relative to the 1991–2020 mean (**Fig. 11a-b**) reveal a pronounced
436 anti-cyclonic circulation (positive anomalies) centered over northern PSEA (~20°N, 100°E) at 500
437 hPa. Similar anti-cyclonic anomalies are also evident in the Z700 field over the BoB. At the same
438 time, significant cyclonic anomalies (negative geopotential height anomalies) are observed over
439 the Arabian Sea and the WNP at both levels. These geopotential height anomaly patterns are
440 broadly consistent with the observed sea surface temperature (SST) anomaly distribution. Positive
441 SST anomalies are evident over the Arabian Sea, whereas negative SST anomalies occur over the
442 BoB (**Fig. 11**). Positive SST anomalies are also observed over the WNP warm pool region, where
443 negative geopotential height anomalies are present. Collectively, these patterns suggest a low–
444 high–low (L–H–L)-like wave train extending from the Arabian Sea to the WNP warm pool region.
445 These findings are consistent with those of Liu et al. (2026), who proposed that enhanced
446 convection over the Horn of Africa and Arabian Peninsula (HAAP) generated downstream Rossby
447 wave propagation across South Asia and mainland Southeast Asia, contributing to anomalous
448 upper-level cyclonic circulation over South Asia and anti-cyclonic circulation over the Indochina
449 Peninsula (ICP) and southern China. However, their analysis was primarily based on upper-
450 tropospheric (~300 hPa) circulation fields. Although our analysis focuses on mid-tropospheric
451 circulation anomalies at 700 and 500 hPa, the observed patterns are broadly consistent with a
452 vertically coherent large-scale circulation response during spring 2023. These circulation
453 anomalies, particularly mid-tropospheric anti-cyclone that suppressed convection over PSEA, are
454 consistent with positive OLR anomalies and reduced precipitation (**Fig. 10**). Subsidence associated
455 with the anti-cyclonic circulation promoted clear-sky conditions (**Fig. 10**) and surface warming,
456 which, together with severe soil moisture deficits, created favorable conditions for intense BB
457 across northern Laos. Liu et al. (2026) further showed that upper-tropospheric convergence and
458 dynamical subsidence associated with this wave pattern contributed to persistent heat and drying
459 over the ICP during spring 2023, potentially supporting the lower- and mid-tropospheric anti-
460 cyclonic anomalies identified here. The circulation pattern also altered regional transport

461 pathways. The combined influence of the WNP cyclone, the BoB anticyclone at 700 hPa, and the
462 PSEA anticyclone at 500 hPa modified the background flow over Southeast Asia. Meridional wind
463 anomalies (**Figs. S11b–c** in the Supplement) show persistent northerly flow over the SCS, enabling
464 southward transport of smoke from northern PSEA toward the SCS and into the southern BoB.
465 Zonal wind anomalies further indicate weakened mid-latitude westerlies and locally reversed
466 easterlies near Japan and Taiwan associated with a strong anti-cyclonic anomaly (**Figs. S11a–b** in
467 the Supplement), suppressing the typical eastward transport of smoke. Consistent with this, AOD
468 observations from the high-altitude mountain background station, namely ‘Lulin Atmospheric
469 Background Station (LABS)’ obtained through AERONET show no notable enhancement in April
470 2023 (**Fig. S12** in the Supplement), indicating reduced smoke transport toward the northwestern
471 Pacific. AERONET comparisons show strong correlations with MODIS AOD: 0.83 for Aqua and
472 0.84 for Terra (**Fig. S13** in the Supplement), further supporting the reliability of the satellite
473 observations as shown in the Dongsha data. Overall, the anomalous circulation pattern,
474 characterized by a BoB anticyclone and a WNP cyclone, redirected BB plumes from northern
475 PSEA toward the SCS and southern BoB, producing the exceptional aerosol loading observed in
476 April 2023.

477 A key question is whether April 2023 was an exceptional BB year relative to PSEA, or
478 whether similar conditions have occurred in other high-BB years. High-BB years were identified
479 using standardized fire anomalies derived from April MODIS fire counts following the method of
480 Vadrevu et al. (2019). For this analysis, April fire counts from 2003–2023 were standardized
481 relative to the 2003–2022 climatology over northern PSEA (17–23°N). Years with anomaly values
482 exceeding 0.5 were classified as high-BB years (**Fig. S14**), including 2003, 2006, 2008, 2010,
483 2014, 2015, 2016, and 2023. Composite analyses of MODIS AOD, 500 hPa geopotential height
484 (Z500), and wind vectors were conducted to characterize typical aerosol and circulation patterns
485 during high-BB conditions. **Figure 12a–c** presents the spatial distributions of composite AOD for
486 high-BB years, AOD during April 2023, and their anomalies, respectively, while **Fig. 12d–f** shows
487 the corresponding Z500 and wind vector fields. Relative to the high-BB composite, April 2023
488 exhibited substantially higher AOD across PSEA, the SCS, and the southern BoB, indicating
489 enhanced regional aerosol loading. The Z500 field further showed pronounced positive anomalies
490 over northern PSEA, reflecting a stronger, more spatially coherent anti-cyclonic circulation than
491 under typical high-BB conditions. Correspondingly, wind anomalies revealed enhanced northerly

492 flow over the SCS during 2023, suggesting strengthened meridional aerosol transport. An
493 additional comparison between April 2016 and April 2023 (**Fig. S15** in the supplement) showed
494 similar spatial patterns, including enhanced AOD over southern PSEA. However, the magnitude
495 and spatial extent of the AOD enhancement were greater in 2023. The AOD anomaly between
496 2023 and 2016 further revealed pronounced increases over the SCS and southern BoB, coinciding
497 with enhanced northerly anomalies. Overall, these results suggest that anomalous circulation
498 conditions in 2023 likely amplified aerosol transport and accumulation beyond those typically
499 associated with high-BB years.



500

501 **Figure 12.** Spatial distribution of MODIS aerosol optical depth (AOD), MERRA-2 500-hPa
 502 geopotential height (Z500), and wind vectors during April. (a) Composite AOD for high biomass-
 503 burning (BB) years, (b) AOD in 2023, and (c) AOD anomalies between 2023 and the composite
 504 high-BB years. Panels (d–f) show the corresponding composites for Z500 and associated wind
 505 vectors for (d) high-BB years, (e) 2023, and (f) anomalies between 2023 and the high-BB
 506 composite, respectively.

507

508 Another question is whether inter-annual variability associated with climate oscillations,
509 such as the El Niño–Southern Oscillation (ENSO), influenced BB activity and circulation in 2023.
510 SST anomalies associated with ENSO strongly modulate Indo-Pacific circulation and hydro-
511 climate, with El Niño events typically enhancing springtime fires through drought, reduced
512 precipitation, and suppressed moisture transport (Yin, 2020; Zhu et al., 2021; Zheng et al., 2023).
513 We constructed composites of MODIS AOD and 500-hPa wind vectors for El Niño–ensuing and
514 La Niña–ensuing Aprils during 2003–2022 (**Fig. S16** in the Supplement). The results reveal higher
515 AOD over northern PSEA and coastal South China during El Niño-ensuing Aprils, accompanied
516 by a stronger anti-cyclonic system over PSEA extending from the BoB, consistent with enhanced
517 aerosol accumulation. In contrast, Aprils following La Niña show weaker circulation and lower
518 AOD. April 2023 occurred during the transition from a triple-dip La Niña to a developing El Niño,
519 deviating from typical ENSO-fire patterns. This unusually large-scale background is consistent
520 with Liu et al. (2026), who noted that the extreme spring 2023 heat event over the ICP differed
521 fundamentally from canonical ENSO-linked events, as severe regional warming and subsidence
522 developed despite antecedent La Niña conditions.

523 Overall, systematic analysis of MODIS fire counts, burned area (BA), HYSPLIT back
524 trajectories, and MERRA-2 large-scale circulation fields, we conclude that the extreme aerosol
525 event in April 2023 was shaped not only by BB activity but also by anomalous large-scale
526 circulation patterns. These findings highlight the combined influence of BB emissions and
527 background meteorological conditions in producing the exceptional smoke event.

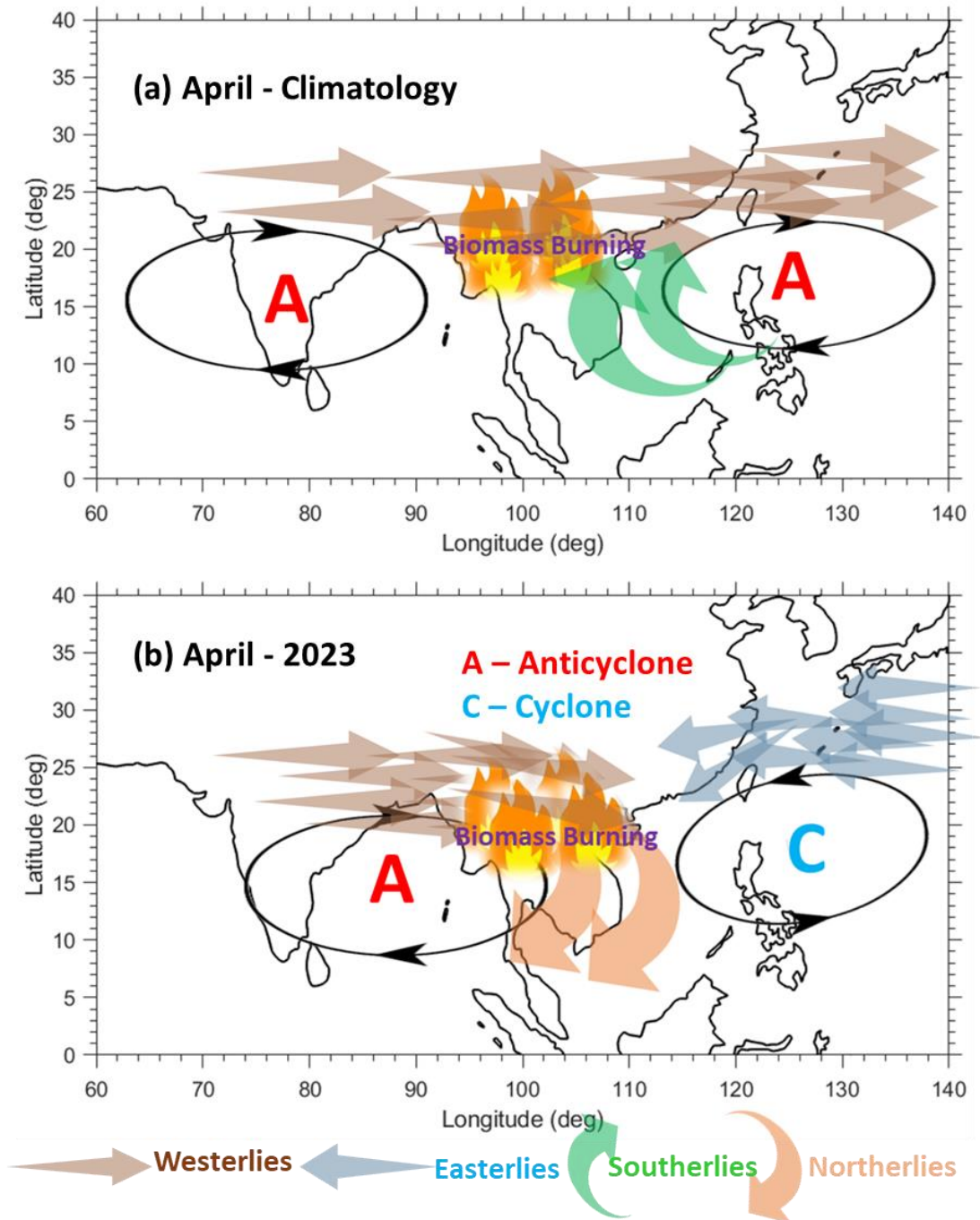
528 **4. Summary and Conclusions**

529 In April 2023, record-breaking aerosol loading was observed over the South China Sea
530 (SCS). By integrating multiple satellite measurements (MODIS, MOPITT, AIRS, and CALIPSO),
531 the MERRA-2 reanalysis, and NOAA HYSPLIT back-trajectory analysis, we systematically
532 investigated the sources, transport pathways, and large-scale dynamical conditions associated with
533 this extreme event. MODIS observations indicate an approximately 150% increase in aerosol
534 optical depth (AOD), relative to the long-term mean (2003-2022). This enhancement was
535 accompanied by pronounced increases in carbon monoxide (CO) in the mid- to lower troposphere
536 (700–500 hPa) as observed by MOPITT and AIRS, consistent with long-range transport of
537 combustion-related pollution. The simultaneous increases in AOD and CO over the remote ocean

538 support the influence of transported biomass-burning (BB) emissions from surrounding source
539 regions. Analysis of MODIS fire counts and burned area revealed a significant enhancement in
540 BB activity over northern PSEA and negligible BB activity over South China and the Maritime
541 Continent. Furthermore, NOAA HYSPLIT back trajectories indicate that most air masses over the
542 SCS originate from the northern PSEA. Together, fire counts, BA, and HYSPLIT trajectory
543 analysis suggest that enhanced BB activity over northern PSEA likely contributed to the
544 exceptional aerosol loading over the SCS in April 2023. Meteorological conditions characterized
545 by suppressed convection, reduced precipitation, elevated surface temperatures, and decreased soil
546 moisture likely promoted increased BB activity. These conditions were associated with a
547 pronounced high-pressure (anti-cyclonic) anomaly over PSEA, as indicated by positive
548 geopotential height anomalies at 500 hPa (**Figure 11a**).

549 Large-scale circulation analyses further reveal a free-tropospheric pattern featuring an
550 eastward-shifted Bay of Bengal (BoB) anticyclone and a western North Pacific (WNP) cyclone
551 (**Figure 11b**). These circulation features significantly modified regional flow over the SCS by
552 reversing the prevailing meridional winds from southerly to northerly anomalies. In addition, the
553 coexistence of a subtropical anticyclone over the northwestern Pacific and the WNP anomaly
554 generated easterly wind anomalies around Taiwan. Together, these anomalous circulation patterns
555 altered BB smoke transport pathways and facilitated aerosol accumulation over the SCS in April
556 2023. A schematic summary of the physical mechanisms is provided in **Figure 13**.

557



558

559 **Figure 13.** Schematic diagram illustrating the physical mechanisms responsible for the record-
 560 breaking aerosol loading over the South China Sea (SCS) in April 2023. The diagram summarizes
 561 the anomalous circulation and transport pathways governing biomass-burning (BB) smoke
 562 distribution. Here, ‘A’ denotes an anticyclone anomaly and ‘C’ denotes a cyclone anomaly.
 563 Horizontal arrows represent subtropical free-tropospheric westerlies and easterlies, while green
 564 and brown arrows indicate southerly and northerly winds, respectively. Top panel: The
 565 climatological conditions in April (1991-2020), characterized by the Bay of Bengal (BoB) and

566 western Pacific anticyclones, as well as prevailing southwesterly and southerly winds over the
567 SCS that favor typical smoke transport toward Taiwan and the western North Pacific (WNP).
568 Bottom panel: April 2023 conditions, featuring a WNP cyclone, and an eastward-shifted BoB
569 anticyclone. These anomalies generated persistent northerly winds over the SCS and redirected
570 BB plumes toward the SCS and the southern BoB. Strengthened easterlies around Taiwan further
571 inhibited eastward transport, resulting in exceptional aerosol accumulation over the SCS in April
572 2023.

573 While this study focuses on the sources, transport pathways, and dynamical drivers of the
574 record aerosol event, its broader impacts remain to be quantified. In particular, aerosol–radiation
575 interactions associated with elevated AOD may significantly affect regional radiative forcing,
576 atmospheric heating profiles, and the hydrological cycle. Future work will quantify the radiative
577 impacts of these extreme aerosol concentrations and assess their implications for regional climate.
578 Additionally, elevated BB emissions of CO and other precursors may enhance tropospheric ozone
579 formation, a topic that warrants further investigation. Notably, mainland Southeast Asia
580 experienced an extreme heatwave in April 2023, with record-high temperatures (Zachariah et al.,
581 2024; Lyu et al., 2024). While previous studies attribute this event to anthropogenic climate
582 change, strengthened high-pressure systems, and land–atmosphere coupling, our results suggest
583 that BB aerosols and associated greenhouse gas emissions may also have contributed to the
584 regional heat anomaly. Key outstanding questions include how BB-derived greenhouse gases
585 influence regional radiative trapping and how elevated aerosol concentrations modify surface
586 radiation, cloud processes, and precipitation. Addressing these questions is essential for
587 understanding compound climate extremes in PSEA and surrounding regions. In conclusion, this
588 study highlights the combined role of BB emissions and large-scale dynamical conditions in
589 shaping smoke transport over Southeast Asia, providing deeper insights into the mechanisms
590 governing extreme regional aerosol events.

591 **Code and data availability**

592 This study exclusively utilized publicly available datasets, and no new observational data were
593 generated. All data required to evaluate the conclusions of this study are included in the paper
594 and/or the Supplementary Information. Most figures presented in this study were generated using
595 MATLAB R2020a. All datasets used in the study are freely available for download from their
596 respective websites. MODIS data available from
597 <https://modis.gsfc.nasa.gov/data/dataproduct/mod08.php> (last access: 11 June 2026). The AIRS and

598 MOPITT CO data can be downloaded from https://disc.gsfc.nasa.gov/datasets/AIRS3STM_7.0
599 (AIRS project, 2019) and https://asdc.larc.nasa.gov/project/MOPITT/MOP02J_8 (NASA, 2023a)
600 (last access: 11 June 2026). MERRA-2 data are available online through the NASA Goddard Earth
601 Sciences Data Information Services Center (GES DISC; <https://disc.gsfc.nasa.gov>; NASA, 2023b)
602 (last access: 11 June 2026). The MODIS fire and burned area products can be downloaded from
603 https://firms.modaps.eosdis.nasa.gov/active_fire/ (NASA, 2023c) (last access: 11 June 2026).
604 Daily CALIPSO vertical distribution images of various aerosol types were obtained from
605 <https://www-calipso.larc.nasa.gov/products> (last access: 11 June 2026). The NOAA HYSPLIT
606 back trajectories are retrieved from <https://www.ready.noaa.gov/HYSPLIT.php> (last access: 11
607 June 2026).

608 **Author Contributions**

609 **SRB:** Conceptualization, Data curation, Formal analysis, Investigation, Software, Validation,
610 Visualization, Writing – original draft preparation, Writing – review and editing; **N-HL:**
611 Conceptualization, Investigation, Funding Acquisition, Supervision, Resources, Writing – review
612 and editing.

613 **Competing interests**

614 The authors declare no competing interests.

615 **Acknowledgements**

616 We acknowledge the National Science and Technology Council of Taiwan for supporting the
617 research under grant 114-2111-M-008-030. The authors thank NASA and NOAA for providing
618 MOPITT, MODIS, CALIPSO and AIRS satellite data. We thank NASA's Global Monitoring and
619 Assimilation Office (GMAO) for providing the Modern-Era Retrospective analysis for Research
620 and Applications, Version 2 (MERRA-2) data.

621 **References**

622 Anderson, T. L., Charlson, R. J., Schwartz, S. E., Knutti, R., Boucher, O., Rodhe, H., and
623 Heintzenberg, J.: Climate forcing by aerosol– a hazy picture, *Science*, 300, 1103–1104,
624 <https://doi.org/10.1126/science.1084777>, 2003.

625 AIRS Project. Aqua/AIRS L3 Monthly Standard Physical Retrieval (AIRS-only) 1 degree x 1
626 degree V7.0 [Data set]. NASA Goddard Earth Sciences Data and Information Services Center.
627 <https://doi.org/10.5067/UBENJB9D3T2H>, 2020.

628 Buchholz, R. R., Worden, H. M., Park, M., Francis, G., Deeter, M. N., Edwards, D. P., Emmons,
629 L. K., Gaubert, B., Gille, J., Martinez-Alonso, S., Tang, W., Kumar, R., Drummond, J. R.,
630 Clerbaux, C., George, M., Coheur, P.-F., Hurtmans, D., Bowman, K. W., Luo, M., Payne, V. H.,
631 Worden, J. R., Chin, M., Levy, R. C., Warner, J., Wei, Z., and Kulawik, S. S.: Air pollution trends
632 measured from Terra: CO and AOD over industrial, fire-prone, and background regions, *Remote*
633 *Sens. Environ.*, 256, 112275, <https://doi.org/10.1016/j.rse.2020.112275>, 2021.

634 Byrne, B., Liu, J., and Bowman, K. W.: Carbon emissions from the 2023 Canadian wildfires,
635 *Nature*, 633, 835–839, <https://doi.org/10.1038/s41586-024-07878-z>, 2024.

636 Chan, C. Y., Chan, L. Y., Harris, J. M., Oltmans, S. J., Blake, D. R., Qin, Y., Zheng, Y. G., and
637 Zheng, X. D.: Characteristic of biomass-burning emission sources, transport, and chemical
638 speciation in enhanced springtime tropospheric ozone profile over Hong Kong, *J. Geophys. Res.*,
639 108, 4015, <https://doi.org/10.1029/2001JD001555>, 2003.

640 Chang, J. H.-W., Wong, Y. J., Ooi, M. C.-G., Babu, S. R., Pani, S. K., and Lin, N.-H.: Biomass-
641 burning in critical fire region over the Maritime Continent from 2012 to 2021: A review of the
642 meteorological influence and cloud-aerosol-radiation interactions, *Atmos. Environ.*, 320, 120324,
643 <https://doi.org/10.1016/j.atmosenv.2023.120324>, 2024.

644 Chuang, M-T., Lee, C-T., Chou, C. C-K., Lin, N-H., Sheu, G-R., Wang, J-L., Chang, S-C., Wang,
645 S-H., Chi, K. H., Young, C-Y., Huang, H., Chen, H-W., Weng, G-H., Lai, S-Y., Hsu, S-P., Chang,
646 Y-J., Chang, J-H., and Wu, X-C.: Carbonaceous aerosols in the air masses transported from
647 Indochina to Taiwan: Longterm observation at Mt. Lulin, *Atmos. Environ.*, 89, 507–516,
648 <https://doi.org/10.1016/j.atmosenv.2013.11.066>, 2014.

649 Cohen, J. B.: Quantifying the occurrence and magnitude of the Southeast Asian fire climatology,
650 *Environ. Res. Lett.*, 9, 114018, <https://doi.org/10.1088/1748-9326/9/11/114018>, 2014.

651 Cohen, J. B., Lecoecur, E., and Hui Loong Ng, D.: Decadal-scale relationship between
652 measurements of aerosols, land-use change, and fire over Southeast Asia, *Atmos. Chem. Phys.*,
653 17, 721–743, <https://doi.org/10.5194/acp-17-721-2017>, 2017.

654

655 Cordero, R. R., Feron, S., Damiani, A., Carrasco, J., Karas, C., Wang, C., Kraamwinkel, C. T., and
656 Beaulieu, A.: Extreme fire weather in Chile driven by climate change and El Niño–Southern
657 Oscillation (ENSO), *Sci. Rep.*, 14, 1974, <https://doi.org/10.1038/s41598-024-52481-x>, 2024.

658 Cui, D., Wang, J., Tan, L., and Dong, Z.: Impact of atmospheric wet deposition on phytoplankton
659 community structure in the South China Sea. *Estuar. Coast. Shelf Sci.* 173: 1–8,
660 <https://doi.org/10.1016/j.ecss.2016.02.011>, 2016.

661 Crutzen, P. J. and Andreae, M. O.: Biomass-burning in the Tropics: Impact on Atmospheric
662 Chemistry and Biogeochemical Cycles, *Science*, 250, 1669–1678,
663 <https://doi.org/10.1126/science.250.4988.1669>, 1990.

664 Deeter, M. N., Edwards, D. P., Francis, G. L., Gille, J. C., Mao, D., Martínez-Alonso, S., Worden,
665 H. M., Ziskin, D., and Andreae, M. O.: Radiance-based retrieval bias mitigation for the MOPITT
666 instrument: the version 8 product, *Atmos. Meas. Tech.*, 12, 4561–4580,
667 <https://doi.org/10.5194/amt-12-4561-2019>, 2019.

668 Dong, Z., Yang, R., Cao, J., Wang, L., and Cheng, J.: A strong high-temperature event in late-
669 spring 2023 in Yunnan province, Southwest China: Characteristics and possible causes. *Atmos.*
670 *Res*, 295, 107017. <https://doi.org/10.1016/j.atmosres.2023.107017>, 2023.

671 Espinoza, J.-C., Jimenez, J. C., Marengo, J. A., Schongart, J., Ronchail, J., Lavado-Casimiro, W.,
672 and Ribeiro, J. V. M.: The new record of drought and warmth in the Amazon in 2023 related to
673 regional and global climatic features, *Sci. Rep.*, 14, 8107, [https://doi.org/10.1038/s41598-024-](https://doi.org/10.1038/s41598-024-58782-5)
674 [58782-5](https://doi.org/10.1038/s41598-024-58782-5), 2024.

675 Fischer, E. M., Seneviratne, S. I., Vidale, P. L., Lüthi, D., and Schär, C.: Soil Moisture –
676 Atmosphere Interactions during the 2003 European Summer Heat Wave, *J. Climate*, 20, 5081–
677 5099, <https://doi.org/10.1175/JCLI4288.1>, 2007.

678 Forster, P., Storelvmo, T., Armour, K., Collins, W., Dufresne, J.-L., Frame, D., Lunt, D. J.,
679 Mauritsen, T., Palmer, M. D., Watanabe, M., Wild, M., and Zhang, H.: The Earth's Energy Budget,
680 Climate Feedbacks, and Climate Sensitivity, in: *Climate Change 2021: The Physical Science*
681 *Basis, Contribution of Working Group I to the Sixth Assessment Report of the Intergovernmental*
682 *Panel on Climate Change*, edited by: Masson-Delmotte, V., Zhai, P., Pirani, A., Connors, S. L.,
683 Péan, C., Berger, S., Caud, N., Chen, Y., Goldfarb, L., Gomis, M. I., Huang, M., Leitzell, K.,
684 Lonnoy, E., Matthews, J. B. R., Maycock, T. K., Waterfield, T., Yelekçi, O., Yu, R., and Zhou,
685 B., Cambridge University Press, Cambridge, United Kingdom and New York, NY, USA, pp. 923–
686 1054, <https://doi.org/10.1017/9781009157896.009>, 2021.

687 Forster, P. M., Smith, C., Walsh, T., Lamb, W. F., Lamboll, R., Hall, B., Hauser, M., Ribes, A.,
688 Rosen, D., Gillett, N. P., Palmer, M. D., Rogelj, J., von Schuckmann, K., Trewin, B., Allen, M.,
689 Andrew, R., Betts, R. A., Borger, A., Boyer, T., Broersma, J. A., Buontempo, C., Burgess, S.,
690 Cagnazzo, C., Cheng, L., Friedlingstein, P., Gettelman, A., Gütschow, J., Ishii, M., Jenkins, S.,
691 Lan, X., Morice, C., Mühle, J., Kadow, C., Kennedy, J., Killick, R. E., Krummel, P. B., Minx, J.
692 C., Myhre, G., Naik, V., Peters, G. P., Pirani, A., Pongratz, J., Schleussner, C.-F., Seneviratne, S.
693 I., Szopa, S., Thorne, P., Kovilakam, M. V. M., Majamäki, E., Jalkanen, J.-P., van Marle, M.,
694 Hoesly, R. M., Rohde, R., Schumacher, D., van der Werf, G., Vose, R., Zickfeld, K., Zhang, X.,
695 Masson-Delmotte, V., and Zhai, P.: Indicators of Global Climate Change 2023: annual update of
696 key indicators of the state of the climate system and human influence, *Earth Syst. Sci. Data*, 16,
697 2625–2658, <https://doi.org/10.5194/essd-16-2625-2024>, 2024.

698 Gelaro, R., McCarty, W., Suarez, M. J., Todling, R., Molod, A., Takacs, L., Randles, C. A.,
699 Darmenov, A., Bosilovich, M. G., Reichle, R., Wargan, K., Coy, L., Cullather, R., Draper, C.,

700 Akella, S., Buchard, V., Conaty, A., da Silva, A. M., Gu, W., Kim, G.-K., Koster, R., Lucchesi,
701 R., Merkova, D., Nielsen, J. E., Partyka, G., Pawson, S., Putman, W., Rienecker, M., Schubert, S.
702 D., Sienkiewicz, M., and Zhao, B.: The Modern-Era Retrospective Analysis for Research and
703 Applications, Version 2 (MERRA-2), *J. Climate*, 30, 5419–5454, [https://doi.org/10.1175/JCLI-D-](https://doi.org/10.1175/JCLI-D-16-0758.1)
704 16-0758.1, 2017.

705 Giglio, L., Csiszar, I., and Justice, C. O.: Global distribution and seasonality of active fires as
706 observed with the Terra and Aqua Moderate Resolution Imaging Spectroradiometer (MODIS)
707 sensors, *J. Geophys. Res.-Biogeo.*, 111, <https://doi.org/10.1029/2005JG000142>, 2006.

708 Giglio, L., Schroeder, W., and Justice, C. O.: The collection 6 MODIS active fire detection
709 algorithm and fire products, *Remote Sens. Environ.*, 178, 31–41,
710 <https://doi.org/10.1016/j.rse.2016.02.054>, 2016.

711 Giglio, L., Boschetti, L., Roy, D. P., Humber, M. L., and Justice, C. O.: The Collection 6 MODIS
712 burned area mapping algorithm and product, *Remote Sens. Environ.*, 217, 72–85,
713 <https://doi.org/10.1016/j.rse.2018.08.005>, 2018.

714 Gill, A. E.: Some simple solutions for heat-induced tropical circulation. *Q. J. R. Meteorol. Soc.*
715 106, 447–462. <https://doi.org/10.1002/qj.49710644905>, 1980.

716 Giles, D. M., Sinyuk, A., Sorokin, M. G., Schafer, J. S., Smirnov, A., Slutsker, I., Eck, T. F.,
717 Holben, B. N., Lewis, J. R., Campbell, J. R., Welton, E. J., Korokin, S. V., and Lyapustin, A. I.:
718 Advancements in the Aerosol Robotic Network (AERONET) Version 3 database— automated near-
719 real-time quality control algorithm with improved cloud screening for Sun photometer aerosol op
720 tical depth (AOD) measurements, *Atmos. Meas. Tech.*, 12, 169–209, [https://doi.org/10.5194/amt-](https://doi.org/10.5194/amt-12-169-2019)
721 12-169-2019, 2019.

722 Gui, Y., Wang, K., Jin, Z., Wang, H., Deng, H., Li, X., Tian, X., Wang, T., Chen, W., Wang, T.,
723 and Piao, S.: The decline in tropical land carbon sink drives high atmospheric CO₂ growth rate in
724 2023, *Natl. Sci. Rev.*, nwae365, <https://doi.org/10.1093/nsr/nwae365>, 2024.

725 Hirsch, E. and Koren, I.: Record-breaking aerosol levels explained by smoke injection into the
726 stratosphere, *Science*, 371, 1269–1274, <https://doi.org/10.1126/science.abe1415>, 2021.

727 Hu, Y., Yue, X., and Tian, C.: Climatic drivers of the Canadian wildfire episode in 2023,
728 *Atmospheric and Oceanic Science Letters*, 17, 100483,
729 <https://doi.org/10.1016/j.aosl.2024.100483>, 2024.

730 Huang, H.-Y., Wang, S.-H., Huang, W.-X., Lin, N.-H., Chuang, M.-T., da Silva, A. M., and Peng,
731 C.-M.: Influence of Synoptic-Dynamic Meteorology on the Long-Range Transport of Indochina
732 Biomass-burning Aerosols, *J. Geophys. Res.-Atmos.*, 125, e2019JD031260,
733 <https://doi.org/10.1029/2019JD031260>, 2020.

734 Huang, H.-Y., Wang, S.-H., Lau, W.K.M., Wang, S.-Y.S., and da Silva, A.M.: Impact of regional
735 climate patterns on the biomass-burning emissions and transport over Peninsular Southeast Asia,
736 2000–2019. *Atmos. Res.* 297, 107067. <https://doi.org/10.1016/j.atmosres.2023.107067>, 2024.

- 737 IPCC: Climate Change 2021 – The Physical Science Basis: Working Group I Contribution to the
738 Sixth Assessment Report of the Intergovernmental Panel on Climate Change, Cambridge
739 University Press, Cambridge, <https://doi.org/10.1017/9781009157896>, 2023.
- 740 Jain, P., Barber, Q. E., Taylor, S. W., Whitman, E., Castellanos Acuna, D., Boulanger, Y.,
741 Chavardès, R. D., Chen, J., Englefield, P., Flannigan, M., Girardin, M. P., Hanes, C. C., Little, J.,
742 Morrison, K., Skakun, R. S., Thompson, D. K., Wang, X., and Parisien, M.-A.: Drivers and
743 impacts of the record-breaking 2023 wildfire season in Canada, *Nature Communications*, 15, 6764,
744 <https://doi.org/10.1038/s41467-024-51154-7>, 2024.
- 745 Jones, M. W., Kelley, D. I., Burton, C. A., Di Giuseppe, F., Barbosa, M. L. F., Brambleby, E.,
746 Hartley, A. J., Lombardi, A., Mataveli, G., McNorton, J. R., Spuler, F. R., Wessel, J. B.,
747 Abatzoglou, J. T., Anderson, L. O., Andela, N., Archibald, S., Armenteras, D., Burke, E.,
748 Carmenta, R., Chuvieco, E., Clarke, H., Doerr, S. H., Fernandes, P. M., Giglio, L., Hamilton, D.
749 S., Hantson, S., Harris, S., Jain, P., Kolden, C. A., Kurvits, T., Lampe, S., Meier, S., New, S.,
750 Parrington, M., Perron, M. M. G., Qu, Y., Ribeiro, N. S., Saharjo, B. H., San-Miguel-Ayanz, J.,
751 Shuman, J. K., Tanpipat, V., van der Werf, G. R., Veraverbeke, S., and Xanthopoulos, G.: State
752 of Wildfires 2023–2024, *Earth Syst. Sci. Data*, 16, 3601–3685, [https://doi.org/10.5194/essd-16-](https://doi.org/10.5194/essd-16-3601-2024)
753 [3601-2024](https://doi.org/10.5194/essd-16-3601-2024), 2024.
- 754 Ke, P., Ciais, P., Sitch, S., Li, W., Bastos, A., Liu, Z., Xu, Y., Gui, X., Bian, J., Goll, D. S., Xi, Y.,
755 Li, W., O'Sullivan, M., Goncalves De Souza, J., Friedlingstein, P., and Chevallier, F.: Low latency
756 carbon budget analysis reveals a large decline of the land carbon sink in 2023, *National Science*
757 *Review*, 11, nwae367, <https://doi.org/10.1093/nsr/nwae367>, 2024.
- 758 Kim, M.-H., Omar, A. H., Tackett, J. L., Vaughan, M. A., Winker, D. M., Trepte, C. R., Hu, Y.,
759 Liu, Z., Poole, L. R., Pitts, M. C., Kar, J., and Magill, B. E.: The CALIPSO version 4 automated
760 aerosol classification and lidar ratio selection algorithm, *Atmos. Meas. Tech.*, 11, 6107–6135,
761 <https://doi.org/10.5194/amt11-6107-2018>, 2018.
- 762 Kolden, C. A., Abatzoglou, J. T., Jones, M. W., and Jain, P.: Wildfires in 2023, *Nat. Rev. Earth*
763 *Environ.*, 5, 238–240, <https://doi.org/10.1038/s43017-024-00544-y>, 2024.
- 764 Lai, G. and Zhang Y.: Increased atmospheric aridity and reduced precipitation drive the 2023
765 extreme wildfire season in Canada. *Geophys. Res. Lett.*, 52, e2024GL114492.
766 <https://doi.org/10.1029/2024GL114492>, 2025.
- 767 Liao, Z. H., Ling, Z. H., Gao, M., Sun, J. R., Zhao, W., Ma, P. K., Quan, J. N., and Fan, S. J.:
768 Tropospheric Ozone Variability Over Hong Kong Based on Recent 20 years (2000–2019)
769 Ozone Sonde Observation, *J. Geophys. Res.-Atmos.*, 126, <https://doi.org/10.1029/2020jd033054>,
770 2021.
- 771 Lemus-Canovas, M., Insua-Costa, D., Trigo, R. M., and Miralles, D. G.: Record-shattering 2023
772 Spring heatwave in western Mediterranean amplified by long-term drought, *npj Climate and*
773 *Atmospheric Science*, 7, 25, <https://doi.org/10.1038/s41612-024-00569-6>, 2024.

774 Lee, C.-T., Ram, S. S., Nguyen, D. L., Chou, C. C., Chang, S.-Y., Lin, N.-H., Chang, S.-C., Hsiao,
775 T.-C., Sheu, G.-R., and Ou-Yang, C.-F.: Aerosol chemical profile of near-source biomass-burning
776 smoke in Sonla, Vietnam during 7-SEAS campaigns in 2012 and 2013, *Aerosol Air Qual. Res.*,
777 16, 2603–2617, 2016.

778 Lin, N.-H., Tsay, S.-C., Maring, H. B., Yen, M.-C., Sheu, G.-R., Wang, S.-H., Chi, K. H., Chuang,
779 M.-T., Ou-Yang, C.-F., Fu, J. S., Reid, J. S., Lee, C.-T., Wang, L.-C., Wang, J.-L., Hsu, C. N.,
780 Sayer, A. M., Holben, B. N., Chu, Y.-C., Nguyen, X. A., Sopajaree, K., Chen, S.-J., Cheng, M.-
781 T., Tsuang, B.-J., Tsai, C.-J., Peng, C.-M., Schnell, R. C., Conway, T., Chang, C.-T., Lin, K.-S.,
782 Tsai, Y. I., Lee, W.-J., Chang, S.-C., Liu, J.-J., Chiang, W.-L., Huang, S.-J., Lin, T.-H., and Liu,
783 G.-R.: An overview of regional experiments on biomass-burning aerosols and related pollutants in
784 Southeast Asia: From BASE-ASIA and the Dongsha Experiment to 7-SEAS, *Atmos. Environ.*, 78,
785 1–19, <https://doi.org/10.1016/j.atmosenv.2013.04.066>, 2013.

786 Lin, C.-Y., Hsu, H.-M., Lee, Y. H., Kuo, C. H., Sheng, Y.-F., and Chu, D. A.: A new transport
787 mechanism of biomass-burning from Indochina as identified by modeling studies, *Atmos. Chem.*
788 *Phys.*, 9, 7901–7911, <https://doi.org/10.5194/acp-9-7901-2009>, 2009.

789 Lin, C. C., Chen, W. N., Loftus, A. M., Lin, C. Y., Fu, Y. T., Peng, C. M., and Yen, M. C.:
790 Influences of the long-range transport of biomass-burning pollutants on surface air quality during
791 7-SEAS field campaigns, *Aerosol Air Qual. Res.*, 17, 2595–2607,
792 <https://doi.org/10.4209/aaqr.2017.08.0273>, 2017.

793 Li, J. Li X. and Ying T.: North Atlantic and the Barents Sea variability contribute to the 2023
794 extreme fire season in Canada. *Proc. Natl Acad. Sci. USA*, 121 (49).
795 <https://doi.org/10.1073/pnas.241424112>, 2024.

796 Liu, H., Jacob, D. J., Chan, L. Y., Oltmans, S. J., Bey, I., Yantosca, R. M., Harris, J. M., Duncan,
797 B. N., and Martin, R. V.: Sources of tropospheric ozone along the Asian Pacific Rim: An analysis
798 of ozonesonde observations, *J. Geophys. Res.*, 107, ACH 3-1-ACH 3-19,
799 <https://doi.org/10.1029/2001JD002005>, 2002.

800 Liu, Z., Deng, Z., Davis, S. J., and Ciais, P.: Global carbon emissions in 2023, *Nature Reviews*
801 *Earth and Environment*, 1–2, <https://doi.org/10.1038/s43017-024-00532-2>, 2024.

802 Liu, B., Fang, Y., Sun, S., Liu, L., and Cheah, W.: Extreme High Temperatures in the Indochina
803 Peninsula and Their Association With Enhanced Convection in the Horn of Africa and Arabian
804 Peninsula During Spring 2023. *Atmospheric Science Letters*. 27, no. 5: e70026.
805 <https://doi.org/10.1002/asl2.70026>, 2026.

806 Lyu, Y., Wang, J., Zhi, X., Wang, X., Zhang, H., Wen, Y., Park, E., Lee, J., Wan, X., Zhu, S.,
807 Dung, D.T.: The characterization, mechanism, predictability, and impacts of the unprecedented
808 2023 Southeast Asia heatwave. *npj Clim. Atmos. Sci.* 7, 246. [https://doi.org/10.1038/s41612-024-](https://doi.org/10.1038/s41612-024-00797-w)
809 [00797-w](https://doi.org/10.1038/s41612-024-00797-w), 2024.

810 Ma, T., Chen, W., Cai, Q., Dong, Z., Wang, L., Hu, P., Gao, L., Garfinkel, C.: Attribution analysis
811 of the persistent and extreme drought in Southwest China during 2022–2023. *Environ. Res. Lett.*
812 <https://doi.org/10.1088/1748-9326/ad8171>, 2024.

813 MacCarthy, J., Tyukavina, A., Weisse, M.J., Harris, N., & Glen, E., Extreme wildfires in Canada
814 and their contribution to global loss in tree cover and carbon emissions in 2023. *Global Change*
815 *Biology*, 30, e17392. doi:10.1111/gcb.17392, 2024.

816 McMillan, W. W., Barnet, C., Strow, L., Chahine, M. T., McCourt, M. L., Warner, J. X., Novelli,
817 P. C., Korontzi, S., Maddy, E. S., and Datta, S.: Daily global maps of carbon monoxide from
818 NASA's Atmospheric Infrared Sounder, *Geophys. Res. Lett.*, 32, L11801,
819 <https://doi.org/10.1029/2004GL021821>, 2005.

820 McMillan, W. W., Evans, K. D., Barnet, C. D., Maddy, E. S., Sachse, G. W., and Diskin, G. S.:
821 Validating the AIRS Version 5 CO retrieval with DACOM in situ measurements during INTEX-
822 A and -B, *IEEE T. Geosci. Remote*, 49, 2802–2813, <https://doi.org/10.1109/TGRS.2011.2106505>,
823 2011.

824 Michailidis, K., Garane, K., Karagiozidis, D., Peletidou, G., Voudouri, K.-A., Balis, D., and Bais,
825 A.: Extreme wildfires over northern Greece during summer 2023 – Part A: Effects on aerosol
826 optical properties and solar UV radiation, *Atmospheric Research*, 311, 107700,
827 <https://doi.org/10.1016/j.atmosres.2024.107700>, 2024.

828 Min, S. K.: Human influence can explain the widespread exceptional warmth in 2023. *Commun.*
829 *Earth Environ.* 5, 215 <https://doi.org/10.1038/s43247-024-01391-x>, 2024.

830 Omar, A. H., Winker, D. M., Vaughan, M. A., Hu, Y., Trepte, C. R., Ferrare, R. A., Lee, K.-P.,
831 Hostetler, C. A., Kittaka, C., Rogers, R. R., Kuehn, R. E., and Liu, Z.: The CALIPSO automated
832 aerosol classification and lidar ratio selection algorithm, *J. Atmos. Ocean. Tech.*, 26, 1994–2014,
833 <https://doi.org/10.1175/2009JTECHA1231.1>, 2009.

834 Ou-Yang, C. F., Lin, N. H., Sheu, G. R., Lee, C. T., and Wang, J. L.: Seasonal and diurnal
835 variations of ozone at a high-altitude mountain baseline station in East Asia, *Atmos. Environ.*, 46,
836 279–288, <https://doi.org/10.1016/j.atmosenv.2011.09.060>, 2012.

837 Ou-Yang, C. F., Lin, N. H., Lin, C. C., Wang, S. H., Sheu, G. R., Lee, C. Te, Schnell, R. C., Lang,
838 P. M., Kawasato, T., and Wang, J. L.: Characteristics of atmospheric carbon monoxide at a high-
839 mountain background station in East Asia, *Atmos. Environ.*, 89, 613–622,
840 <https://doi.org/10.1016/j.atmosenv.2014.02.060>, 2014.

841 Ou-Yang, C. F., Ravindra Babu, S., Lee, J.-R., Yen, M.-C., Griffith, S. M., Lin, C.-C., Chang, S.-
842 C., and Lin, N.-H.: Detection of stratospheric intrusion events and their role in ozone enhancement
843 at a mountain background site in sub-tropical East Asia, *Atmos. Environ.*, 268, 118779,
844 <https://doi.org/10.1016/j.atmosenv.2021.118779>, 2022.

845 Pani, S. K., Wang, S. H., Lin, N. H., Lee, C. Te, Tsay, S. C., Holben, B. N., Janjai, S., Hsiao, T.
846 C., Chuang, M. T., and Chantara, S.: Radiative effect of springtime biomass-burning aerosols over
847 northern Indochina during 7-SEAS/BASELInE 2013 campaign, *Aerosol Air Qual. Res.*, 16, 2802–
848 2817, <https://doi.org/10.4209/aaqr.2016.03.0130>, 2016.

849 Pani, S. K., Ou-Yang, C.-F., Wang, S.-H., Ogren, J. A., Sheridan, P. J., Sheu, G.-R., and Lin, N.-
850 H. J. A. E.: Relationship between long-range transported atmospheric black carbon and carbon
851 monoxide at a high-altitude background station in East Asia, *Atmos. Environ.*, 210, 86–99,
852 <https://doi.org/10.1016/j.atmosenv.2019.04.053>, 2019.

853 Pani, S.K., Huang, H.-Y., Wang, S.-H., Holben, B.N., Lin, N.-H.: Long-term observation of
854 columnar aerosol optical properties over the remote South China Sea. *Sci. Total Environ.* 905,
855 167113 <https://doi.org/10.1016/j.scitotenv.2023.167113>, 2023.

856 Platnick, S., King, M. and Hubanks, P.: MODIS Atmosphere L3 Monthly Product.
857 https://doi.org/10.5067/MODIS/MOD08_M3.006, 2015.

858 Perkins-Kirkpatrick, S., Barriopedro, D., Jha, R., Wang, L., Mondal, A., Libonati, R., and
859 Kornhuber, K.: Extreme terrestrial heat in 2023, *Nature Reviews Earth & Environment*, 5, 244–
860 246, <https://doi.org/10.1038/s43017-024-00536-y>, 2024.

861 Raghuraman, S. P., Soden, B., Clement, A., Vecchi, G., Menemenlis, S., and Yang, W.: The 2023
862 global warming spike was driven by the El Niño–Southern Oscillation, *Atmos. Chem. Phys.*, 24,
863 11275–11283, <https://doi.org/10.5194/acp-24-11275-2024>, 2024.

864 Ramanathan, V., Crutzen, P. J., Kiehl, J. T., and Rosenfeld, D.: Aerosols, climate, and the
865 hydrological cycle, *Science*, 294, 2119–2124, <https://doi.org/10.1126/science.1064034>, 2001.

866 Ravindra Babu, S., Ou-Yang, C.-F., Griffith, S. M., Pani, S. K., Kong, S. S.-K., and Lin, N.-H.:
867 Transport pathways of carbon monoxide from Indonesian fire pollution to a subtropical high-
868 altitude mountain site in the western North Pacific, *Atmos. Chem. Phys.*, 23, 4727–4740,
869 <https://doi.org/10.5194/acp-23-4727-2023>, 2023.

870 Ravindra Babu, S. and Lin, N.-H.: Changing pattern of springtime biomass-burning over Peninsular
871 Southeast Asia (PSEA) in recent decades. *ESS Open Archive* . August 08, 2023. DOI:
872 10.22541/essoar.169111389.92212046/v2, 2023.

873 Reid, J. S., Hyer, E. J., Johnson, R., Holben, B. N., Yokelson, R. J., Zhang, J., Campbell, J. R.,
874 Christopher, S. A., Di Girolamo, L., Giglio, L., Holz, R. E., Kearney, C., Miettinen, J., Reid, E.
875 A., Turk, F. J., Wang, J., Xian, P., Zhao, G., Balasubramanian, R., Chew, B. N., Janai, S., Lagrosas,
876 N., Lestari, P., Lin, N.-H., Mahmud, M., Nguyen, A. X., Norris, B., Oahn, N. T. K., Oo, M.,
877 Salinas, S. V., Welton, E. J., Liew, S. C.: Observing and understanding the Southeast Asian aerosol
878 system by remote sensing: An initial review and analysis for the Seven Southeast Asian Studies
879 (7SEAS) program, *Atmos. Res.*, 122, 403–468, <https://doi.org/10.1016/j.atmosres.2012.06.005>,
880 2013.

881 Roy, D. P., De Lemos, H., Huang, H., Giglio, L., Houborg, R. and Miura, T.: Multi-resolution
882 monitoring of the 2023 Maui wildfires, implications and needs for satellite-based wildfire disaster
883 monitoring. *Sci. Remote Sens.* 10, 100142. <https://doi.org/10.1016/j.srs.2024.100142>, 2024.

884 Sayer, A. M., Munchak, L. A., Hsu, N. C., Levy, R. C., Bettenhausen, C., and Jeong, M. J.:
885 MODIS collection 6 aerosol products: comparison between Aqua's e-Deep Blue, Dark Target, and
886 “merged” datasets, and usage recommendations, *J. Geophys. Res. Atmos.*, 119, 13965–13989,
887 2014.

888 Seneviratne, S. I., Zhang, X., Adnan, M., Badi, W., Dereczynski, C., Di Luca, A., Ghosh, S.,
889 Iskandar, I., Kossin, J., Lewis, S., Otto, F., Pinto, I., Satoh, M., Vicente-Serrano, S. M., Wehner,
890 M., and Zhou, B.: Weather and Climate Extreme Events in a Changing Climate. In Proc. *Climate*
891 *Change 2021: The Physical Science Basis*. Contribution of Working Group I to the Sixth
892 Assessment Report of the Intergovernmental Panel on Climate Change, 1513–1766 (Cambridge
893 University Press, 2021). <https://doi.org/10.1017/9781009157896.013>, 2021

894 Sheu, G.-R., Lin, N.-H., Wang, J.-L., Lee, C.-T., Ou Yang, C.-F., and Wang, S.-H.: Temporal
895 distribution and potential sources of atmospheric mercury measured at a high-elevation
896 background station in Taiwan, *Atmos. Environ.*, 44, 2393–2400,
897 <https://doi.org/10.1016/j.atmosenv.2010.04.009>, 2010.

898 Sinyuk, A., Holben, B. N., Eck, T. F., Giles, D. M., Slutsker, I., Korkin, S., Schafer, J. S., Smirnov,
899 A., Sorokin, M., and Lyapustin, A.: The AERONET Version 3 aerosol retrieval algorithm,
900 associated uncertainties and comparisons to Version 2, *Atmos. Meas. Tech.*, 13, 3375–3411,
901 <https://doi.org/10.5194/amt-13-3375-2020>, 2020.

902 Torbenson, M. and Büntgen, U.: summer warmth unparalleled over the past 2,000 years. *Nature*
903 631, 94–97 (2024). <https://doi.org/10.1038/s41586-024-07512-y>, 2023.

904 Tsay, S. C., Maring, H. B., Lin, N. H., Buntoung, S., Chantara, S., Chuang, H. C., Gabriel, P. M.,
905 Goodloe, C. S., Holben, B. N., Hsiao, T. C., Christina Hsu, N., Janjai, S., Lau, W. K. M., Lee, C.
906 Te, Lee, J., Loftus, A. M., Nguyen, A. X., Nguyen, C. M., Pani, S. K., Pantina, P., Sayer, A. M.,
907 Tao, W. K., Wang, S. H., Welton, E. J., Wiriya, W., and Yen, M. C.: Satellitesurface perspectives
908 of air quality and aerosol-cloud effects on the environment: An overview of 7-SEAS/BASELInE,
909 *Aerosol Air Qual. Res.*, 16, 2581–2602, <https://doi.org/10.4209/aaqr.2016.08.0350>, 2016.

910 Twomey, S.: The Influence of Pollution on the Shortwave Albedo of Clouds, *Journal of*
911 *Atmospheric Sciences*, 34, 1149–1152, [https://doi.org/10.1175/1520-](https://doi.org/10.1175/1520-0469(1977)034<1149:TIOPOT>2.0.CO;2)
912 [0469\(1977\)034<1149:TIOPOT>2.0.CO;2](https://doi.org/10.1175/1520-0469(1977)034<1149:TIOPOT>2.0.CO;2), 1977.

913 Vadrevu, K. P., Lasko, K., Giglio, L., Schroeder, W., Biswas, S., and Justice, C.: Trends in
914 Vegetation fires in South and Southeast Asian Countries, *Sci. Rep.*, 9, 7422,
915 <https://doi.org/10.1038/s41598-019-43940-x>, 2019.

916 Wang, S., Guan, L., Cohen, J.B., and Qin, K.: Reconstructing top-down global black carbon
917 emissions using remote sensing and models, *Atmospheric Pollution Research*, 16, 10, (102633).
918 <https://doi.org/10.1016/j.apr.2025.102633>, 2025.

919 Wang, S., Cohen, J. B., Deng, W., Qin, K., and Guo, J.: Using a New Top-Down Constrained
920 Emissions Inventory to Attribute the Previously Unknown Source of Extreme Aerosol Loadings
921 Observed Annually in the Monsoon Asia Free Troposphere, *Earths Fut.*, 9, e2021EF002167,
922 <https://doi.org/10.1029/2021EF002167>, 2021.

923 Wang, S., Cohen, J. B., Guan, L., Lu, L., Tiwari, P., & Qin, K.: Observationally constrained global
924 NO_x and CO emissions variability reveals sources which contribute significantly to CO₂
925 emissions, *npj Climate and Atmospheric Science*, 10.1038/s41612-025-00977-2, 8, 1, 2025.

926 Warner, J. X., Comer, M. M., Barnet, C. D., McMillan, W. W., Wolf, W., Maddy, E., and Sachse,
927 G.: A Comparison of Satellite Tropospheric Carbon Monoxide Measurements from AIRS and
928 MOPITT During INTEX-A, *J. Geophys. Res.*, 112, D12S17,
929 <https://doi.org/10.1029/2006JD007925>, 2007.

930 Warner, J., Carminati, F., Wei, Z., Lahoz, W., and Attié, J.-L.: Tropospheric carbon monoxide
931 variability from AIRS under clear and cloudy conditions, *Atmos. Chem. Phys.*, 13, 12469–12479,
932 <https://doi.org/10.5194/acp-13-12469-2013>, 2013.

933 Wai, K. M., Lin, N., Wang, S., and Dokiya, Y.: Rainwater chemistry at a high-altitude station, Mt.
934 Lulin, Taiwan: Comparison with a background station, Mt. Fuji, *J. Geophys. Res.-Atmos.*, 113,
935 D06305, <https://doi.org/10.1029/2006JD008248>, 2008.

936 Wei, J., Li, Z., Peng, Y., and Sun, L.: MODIS Collection 6.1 aerosol optical depth products over
937 land and ocean: validation and comparison, *Atmos. Environ.*, 201, 428–440, 2019a.

938 Wei, J., Li, Z., Sun, L., Peng, Y., and Wang, L.: Improved merge schemes for MODIS Collection
939 6.1 Dark Target and Deep Blue combined aerosol products, *Atmos. Environ.*, 202, 315–327,
940 2019b.

941 Worden, H., Deeter, M., Edwards, D., Gille, J., Drummond, J., and Nédélec, P.: Observations of
942 near-surface carbon monoxide from space using MOPITT multispectral retrievals, *J. Geophys.
943 Res.-Atmos.*, 115, D18314, <https://doi.org/10.1029/2010JD014242>, 2010.

944 Xia, L., Liu, R., Fan, W., and Ren, C.: Emerging carbon dioxide hotspots in East Asia identified
945 by a top-down inventory, *Commun. Earth Environ.*, 6, 1–13, <https://doi.org/10.1038/s43247-024-01991-7>, 2025.

947 Yadav, I. C., Linthoingambi Devi, N., Li, J., Syed, J. H., Zhang, G., and Watanabe, H.: Biomass-
948 burning in Indo-China peninsula and its impacts on regional air quality and global climate change
949 – a review, *Environ. Pollut.*, 227, 414–427, <https://doi.org/10.1016/j.envpol.2017.04.085>, 2017.

950 Zachariah, M., Vautard, R., Chaithra, S. T., Kimutai, J., Arulalan, T., AchutaRao, K., Otto, F. E.
951 L.: Extreme humid heat in South and Southeast Asia in April 2023, largely driven by climate

952 change, detrimental to vulnerable and disadvantaged communities. World Weather Attribution.
953 <https://doi.org/10.25561/104092>, 2023.

954

955

956